Title

P3HT-based solar cells: Structural properties and photovoltaic performance

Authors

Moulé, AJ
Neher, D
Turner, ST

Publication Date

2014

DOI

10.1007/12_2014_289

Peer reviewed

Adv Polym Sci
DOI: 10.1007/12_2014_289

P3HT-Based Solar Cells: Structural Properties and Photovoltaic Performance

Adam J. Moulé, Dieter Neher, and Sarah T. Turner

Abstract Each year we are bombarded with B.Sc. and Ph.D. applications from students that want to improve the world. They have learned that their future depends on changing the type of fuel we use and that solar energy is our future. The hope and energy of these young people will transform future energy technologies, but it will not happen quickly. Organic photovoltaic devices are easy to draw, but the materials, processing steps, and ways of measuring the properties of the materials are very complicated. It is not trivial to make a systematic measurement that will change the way other research groups think or practice. In approaching this chapter, we thought about what a new researcher would need to know about organic photovoltaic devices and materials in order to have a good start in the subject. Then, we simplified that to focus on what a new researcher would need to know about poly-3-hexylthiophene:phenyl-C61-butyric acid methyl ester blends (P3HT:PCBM) to make research progress with these materials. This chapter is by no means authoritative or a compendium of all things on P3HT:PCBM. We have selected to explain how the sample fabrication techniques lead to control of morphology and structural features and how these morphological features have specific optical and electronic consequences for organic photovoltaic device applications.

Keywords Free carrier generation · Non-geminate recombination · Organic solar cells

A.J. Moulé (✉)
Department of Chemical Engineering and Material Science, University of California – Davis, Davis, CA 95616, USA
e-mail: amoule@ucdavis.edu

D. Neher (✉) and S.T. Turner
Institute of Physics and Astronomy, University of Potsdam, Karl-Liebknecht-Str. 24-25, 14476 Potsdam-Golm, Germany
e-mail: neher@uni-potsdam.de

Contents

1 Introduction

Increasing signs of global warming such as recent atmospheric CO_2 levels measured above 400 ppm, polar ice sheet loss, and super-storms, have recently focused attention on short- and long-term solutions to combat climate change [1–4]. Similar to the gold rush in the 1800s and the oil boom in the 1900s, intellectual property on new technologies is now the boom industry for innovative people to become rich and influential fast. In the twenty-first century, scientists and engineers are the pioneers and our ideas are the prize. One of the most alluring energy technologies of the past decade has been organic photovoltaics (OPV). This technology is alluring because it could potentially reduce the cost of producing photovoltaic (PV) modules and thereby make solar energy cost-competitive with fossil fuels. As can be seen in Fig. 1, the allure of OPV brought thousands of scientists and engineers into this new field, generating an exponential increase in scientific knowledge (as measured by the number of scientific articles) in this area. The AU4
sharp focus on OPV technology has led to an explosion of interest in enabling technologies such as polymer synthesis, polymer physics, microstructural measurement techniques, multiscale modeling, photophysics, organic electronics, organic–inorganic hybrid materials, etc. All of this intense focus into one research area has also created intense competition between research groups. With so many new scientific articles published yearly, it is impossible to read them all, and repeat or redundant articles have become unfortunately and unavoidably common. Even review articles and books about OPV have proliferated, making production of an original perspective difficult and a complete literature review impractical. We apologize in advance if any important work is not cited here.

Under this backdrop, we have decided to produce an article that is designed to be helpful to students and postdocs who are entering this field. Rather than focusing on the efficiency of devices or the morphology of materials (subjects that are covered very well elsewhere), we instead focus some attention on how to approach OPV research from a more practical (laboratory-based) perspective. Section 1 introduces

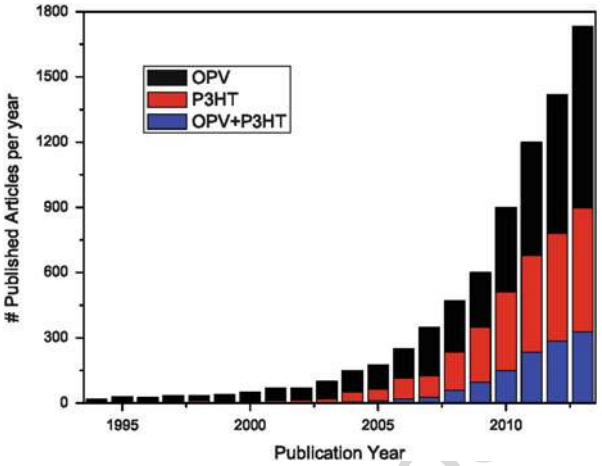

Fig. 1 Number of articles that are found on Web of Science when searching under the topics "Organic photovoltaic", "P3HT", and "OPV + P3HT"

OPV devices, modules, and scale-up. Section 2 discusses fabrication of poly-3-hexylthiophene (P3HT)-based OPV layers, with a focus on practical aspects like how to choose a solvent and how this choice affects other aspects of fabrication. Essentially, this chapter addresses the experimental process of controlling morphology in a P3HT:PCBM blend film, without dwelling on a discussion of the actual morphology of any particular film. Section 3 describes how optical absorption spectra provide detailed information on the crystallization of P3HT in blends with PCBM. Finally, Sect. 4 contains a detailed discussion on the elementary processes involved in photocurrent generation, and how photocurrent losses are related to blend morphology.

1.1 Device Characteristics

A photodiode or PV device converts light energy into electrical energy. The energy of a photon can be expressed by the simple formula:

$$E = hv = \frac{hc}{\lambda}, \tag{1}$$

where E is energy, h is Planck's constant, v is frequency, c is the speed of light, and λ is wavelength. The sun emits photons over a wide energy range in a spectrum that is close to a black body spectrum of ~6,000 K when measured in space. Some of the light is absorbed by the atmosphere by molecules such as O_3, O_2, H_2O, CH_4, and CO_2 or scattered by dust, clouds or pollution. The light spectrum that reaches the earth's surface is for these reasons somewhat different at every place and, due to weather and the rotation of the planet, changes constantly. For the sake of settling arguments, scientists have agreed to test PV devices using an approximate spectrum

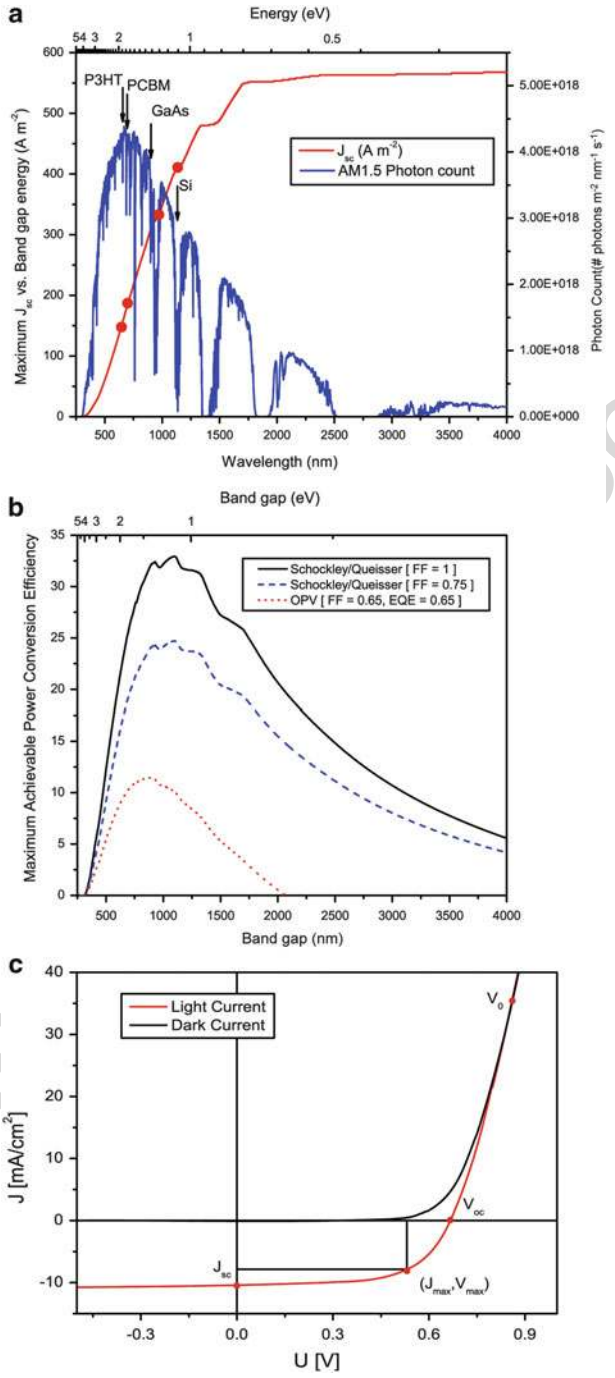

Fig. 2 (**a**) AM1.5G spectrum and calculated maximum J_{sc} as a function of band gap energy. (**b**) Calculated maximum PCE versus band gap energy of a PV device assuming detailed balance

called AM1.5G (Fig. 2a). This spectrum is equivalent to the sun's spectrum at a tilt of 48.2°, which increases the path length through the atmosphere by 150% with respect to 0° incidence. On a sunny day, the total sun power is approximately 930 W/m^2 and includes scattered light from clouds and pollution. This spectrum is approximated using a Xe arc lamp and an optical filter. The Xe lamp solar-simulated spectrum is relatively accurate throughout the visible range but does not have full spectral coverage in the near infrared. Usually solar simulator lamps are calibrated to 1,000 W/m^2 and direct incidence (0°) is used to simplify the experiment. A detailed (and worth reading) description of how to properly measure the mismatch factor for a simulated solar spectrum can be found in a publication by Shrotriya et al. [5]. The standard PCE measurement and testing protocol has also been published [6].

A PV device is made from a semiconductor with an optical band gap (E_g). This E_g is the minimum energy at which electromagnetic energy absorbed within the semiconductor promotes an electron from the valence band to the conduction band. In the case of an OPV device, the excited states are localized onto one or more molecular species, so extended energy bands do not exist. Instead, E_g is the minimum energy needed to promote an electron from the highest occupied molecular orbital (HOMO) to the lowest unoccupied molecular orbital (LUMO) of the molecules or polymers in the film. The band gap sets the maximum short-circuit photocurrent (J_{sc}) and power conversion efficiency (PCE) that any PV device can attain. Photons with energy below E_g do not contribute to photocurrent production. The maximum J_{sc} is shown in Fig. 2a. Due to the principle of detailed balance, the E_g also sets the maximum possible potential at which a photocurrent can be extracted [7]. The combination of these two limitations means that, at best, only ~33% of the total solar power $P(E)$ in the solar spectrum could be collected and converted to electricity by a single junction PV device. Practical considerations like the necessity of a p/n junction, finite area, recombination, reflection, imperfect materials, and series resistance mean that record laboratory scale efficiencies are ~25 and ~28% for single crystalline Si and GaAs, respectively. Figure 2b shows the relationship between band gap and maximum attainable PV efficiency at one sun power given several different assumptions.

The PCE is commonly obtained by measuring the current density (J) versus the applied potential (V) for a PV device under AM1.5G illumination. Figure 2c shows a typical J/V curve for an OPV device based on the donor P3HT and the acceptor phenyl-C61-butyric acid methyl ester (PCBM). The current density measured at zero applied potential is the short-circuit current density (J_{sc}). The applied voltage necessary to drive the current to zero is the open-circuit voltage (V_{oc}). The PCE is determined by calculating the maximum power produced, which is the maximum product of $J \times V$ and is denoted by J_{max} and V_{max}:

Fig. 2 (continued) (*black*), detailed balance and a FF of 0.75 (*blue*), and OPV conditions of 0.6 V energy loss, 0.65 EQE and 0.65 FF. (**c**) *J/V* curve for a P3HT:PCBM OPV device

$$\mathrm{PCE} = \frac{J_{\max} \cdot V_{\max}}{P_{\mathrm{in}}} = \frac{J_{\mathrm{sc}} \cdot V_{\mathrm{oc}} \cdot \mathrm{FF}}{P_{\mathrm{in}}} \tag{2}$$

and the fill factor (FF) is:

$$\mathrm{FF} = \frac{J_{\max} \cdot V_{\max}}{J_{\mathrm{sc}} \cdot V_{\mathrm{oc}}} \tag{3}$$

The device PCE can therefore be increased by increasing the J_{sc} through capture of more photons or reduced recombination, by increasing V_{oc} to approach E_g, and by increasing FF. The *J*/*V* curve for OPV devices has been interpreted in a number of ways and with numerous and sometimes contradictory models. We will discuss fundamental aspects of these models in Sect. 3.

A second measure of efficiency is the external quantum efficiency (EQE), which is the probability that a photon, incident on a PV device, with a wavelength λ will produce a quantum of photocurrent. The EQE can be broken into two components. The optical component is the probability with which a photon is absorbed into the active layer of the PV device η_{abs} and the electrical component is the probability with which the absorbed energy produces photocurrent η_{elec} at the measured bias. Component η_{elec} has been broken into various substeps, each with a particular meaning in several well-cited publications [8]. For this section, we will simply state that η_{elec} is also written as the internal quantum efficiency (IQE):

$$\mathrm{EQE}(\lambda) = \eta_{\mathrm{abs}}(\lambda) \cdot \eta_{\mathrm{elec}}(\lambda) = \eta_{\mathrm{abs}}(\lambda) \cdot \mathrm{IQE}(\lambda) \tag{4}$$

OPV materials that can operate with a band gap of 1.1–1.3 eV have, so far, not been made. Several successful donor polymers have been synthesized that absorb light to energies as low as 1.3 eV. But the most commonly used acceptor, PCBM, has a band gap of 1.75 eV, which is ultimately the limiting factor for efficiency [9]. Several different electrical device models have been used to calculate the maximum possible PCE of an OPV device [9–11]. All three models give a maximum PCE for a single junction device of 10–11%. The model by Veldman et al. predicts the maximum possible V_{oc} to be [9]:

$$V_{\mathrm{oc}}(\mathrm{maximum}) = E_{\mathrm{g}}(\mathrm{PCBM}) - 0.6\ \mathrm{V}. \tag{5}$$

To our knowledge, a higher V_{oc} has never been recorded. The device models predicting 10–11% PCE all assume that the FF would be 0.6–0.65 and that the EQE is 60–65% for photons above E_g. These are quite reasonable assumptions with "hero" devices regularly showing EQE of ~70% and FF of 70%. Considering that the current world record efficiency for an OPV device is 9.1% for a single bulk-heterojunction (BHJ) layer [12], it is reasonable to expect further device records with new materials that approach and exceed 11% PCE.

1.2 Scale-Up and Other Challenges

One exciting aspect of OPV research is the knowledge that there is a direct link between increasing basic science knowledge and progress towards a marketable product. But what does this product look like? What makes it marketable? The goal is to fabricate a PV module with 10–15% PCE that is printed from solution onto a flexible support in a continuous manner, similarly to printing newspapers. This OPV device needs to be inexpensive, lightweight, flexible, and must last for more than 5 years.

The most thorough publication to address the scale-up of OPV is a book by Frederick Krebs [13]. In this book and in follow-up articles, Krebs explores the use of several reel-to-reel printing methods with OPV materials [14–19]. Several other groups are working on continuous coating methods for OPV [20–29]. One of the more pressing problems for the OPV field is that most laboratory work is carried out using spin-coaters and rigid substrates, whereas any expected application of the research will use reel-to-reel coating and flexible substrates [30]. For this reason, future research work should focus on blends prepared by blade coating, which can more easily be compared to a reel-to-reel coated device. Also, blade coaters are more efficient in the use of material, so new polymers can be investigated more efficiently. Another issue is that flexible substrates such as PET–ITO (polyethylene terephthalate coated with indium tin oxide) tend to crack and degrade when bent, which defeats the advantage of flexibility. Flexible substrates are also not as well sealed to prevent O_2 and H_2O penetration of the device. All of these issues show that more studies on OPV device longevity for more device geometries, and the causes of degradation for each geometry, are needed.

1.3 A (Very) Brief History of P3HT:PCBM Solar Cells

Unlike traditional inorganic semiconductors, conjugated organic materials have tightly bound excited states. As a result, light excitation does not result in separated charges, but instead tightly bound exciton states are formed with photoexcitation above the band gap. These excitons recombine quickly (picoseconds to milliseconds), making single-component conjugated organics very inefficient PV materials. In 1986, Tang demonstrated that excitons could be effectively split into separated holes and electrons at a bilayer interface between electron-rich (donor) and electron-poor (acceptor) materials [31]. It was later shown that fullerenes make ideal electron acceptors, but the device efficiencies that could be reached were limited by the short exciton diffusion length [32]. The real breakthrough for OPV applications was the discovery that fullerenes and conjugated polymers could be mixed together to form a mixed bulk-heterojunction (BHJ) layer in which donors and acceptors are in intimate contact and separated charges must navigate through a disordered (mixed) material to

reach the electrodes [33, 34]. All OPV efficiency records since have come from BHJ style devices.

In 2003, Padinger and Sariciftci published a paper reporting a record OPV PCE of 3.5% [35]. This was a huge improvement over the previous record of 2.5% [36], but that was not what made the paper exciting. The exciting pieces of information were:

1. More than one polymer (P3HT instead of MDMO-PPV) made effective OPV devices
2. Choice of solvent and post-processing annealing conditions could greatly affect the device efficiency
3. This improvement was most probably related to the microstructure

The first piece of information spurred a creative explosion in conjugated polymer synthesis that has produced numerous polymers yielding higher OPV efficiencies than P3HT [37–39]. The realization that morphology and device efficiency are intimately related resulted in rapid advances in the use of new instrumentation to study organic nanostructure [40, 41]. At the same time, further OPV device efficiency increases were realized by the use of optimized morphology-controlling strategies including the use of thermal annealing [42], solvent annealing [43], and the application of various co-solvent additives [44, 45]. The most cited paper in all of OPV research (>2,900 total) was published by Li et al. [43]. It demonstrated the change in morphology associated with thermal and solvent annealing and was the first published and certified efficiency record of over 4% for an OPV device. Figure 3 shows *J*/*V* curves of P3HT:PCBM OPV devices from this seminal paper. In the same month, two other groups also published >4% efficiency with P3HT:PCBM but with different composition ratio, layer thickness, and annealing treatment [42, 46]. Although the OPV field has expanded widely beyond the P3HT:PCBM system, P3HT:PCBM remains the "fruit fly" of OPV because the materials are widely available with sufficient purity, and because all manner of new processing techniques can be tested with the knowledge that small changes to the microstructure yield large changes in OPV device PCE.

To demonstrate the pervasive study of P3HT as a model polymer for OPV, we tracked the number of articles published about P3HT and OPV. In Fig. 1 we show the number of scientific papers (as counted by Web of Knowledge) published per year under the search terms "organic photovoltaic", "P3HT", and "organic photovoltaic + P3HT". This search shows that in 2013, more than 300 out of almost 1,700 OPV papers were searchable with P3HT as the OPV polymer, although P3HT has not been a record polymer since 2006. Many of the other more than 500 P3HT articles involve microstructural or photophysical studies that inform the OPV field.

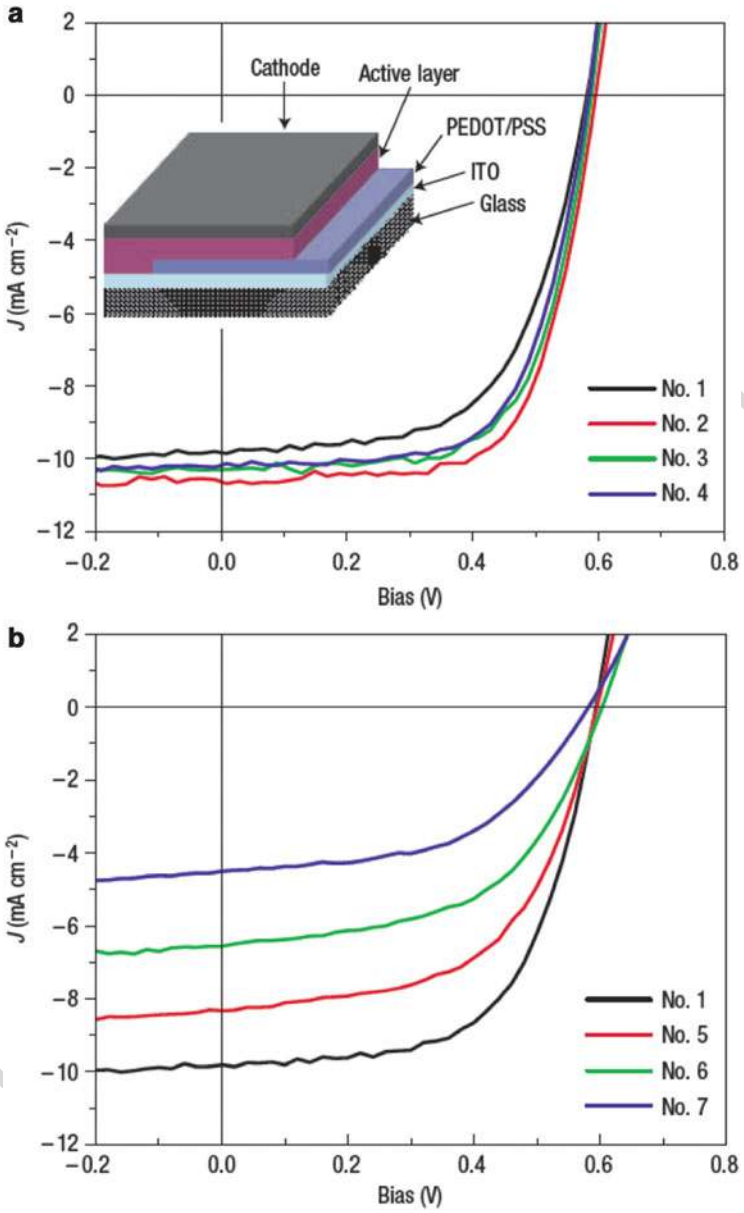

Fig. 3 (**a**) Different *J*/*V* curves of P3HT:PCBM cells corresponding to devices with active layers before (*no. 1*) and after thermal annealing at 110°C for 10 min (*no. 2*), 20 min (*no. 3*), and 30 min (*no. 4*). The active layer thickness was ∼210 nm and the film growth time was ∼20 min. (**b**) *J*/*V* characteristics under illumination for devices with different film growth rates by varying the solvent evaporation time, t_{evp}. The t_{evp} for different films were 20 min (*no. 1*), 3 min (*no. 5*), 40 s (*no. 6*), and 20 s (*no. 7*). Reprinted with permission from [43]. Copyright© 2005, Rights Managed by Nature Publishing Group

2 Relating Processing Conditions to Bulk-Heterojunction Morphology

One of the stranger lessons to be gleaned from the study of P3HT:PCBM is that the keys to understanding and controlling P3HT:PCBM BH) morphology were published in 1993 [47] and 1994 [48], before the BHJ concept had been introduced [32–34]. The 1993 paper showed a transmission electron microscopy (TEM) image and crystal structure for a self-assembled P3HT nanoribbon. The 1994 paper reported on the solvatochromic and thermochromic properties of P3HT and related the folding of P3HT, due to reduced temperature or poor solvent, to the strong red shift in the absorption spectrum.

It is very instructive that in 1993 the strong tendency for P3HT to form ribbon-like nanostructures was known. Also, the solvents necessary to crystallize P3HT, the techniques to measure the fibers, and the technique to separate and coat the fibers were all known. In 1994 the research community knew that poor solvents caused P3HT to form supramolecular structures with coplanar P3HT chains and that this resulted in a red shift of the absorption spectrum and formation of vibronic structure. It was known that the same structures result from cooling a P3HT melt. But nevertheless, the research community did not start using these ideas to control P3HT:PCBM morphology until a decade later.

Why not?

The P3HT:PCBM processing conditions did not create a linear and obvious change in morphology and so the relationship between processing conditions and morphology to OPV performance was not obvious. The rest of this section points out the various relationships between processing conditions and the final film morphology. Many new OPV polymers exist that have higher efficiency than P3HT:PCBM. In terms of processability, these newer polymers may be more or less soluble, have lower or higher tendency crystallize, or have differing mutual solubility with the fullerene of choice. The discussion focuses on the processing lessons that can be broadly applied to a variety of OPV materials.

2.1 The Fabrication Toolkit

This section was written from the perspective of a device physicist and is designed to help graduate students with new OPV materials. From this perspective, polymers and fullerenes arrive at the laboratory in small quantities and one wishes to learn whether this new material might be a good candidate for OPV devices. Usually, the synthesis group supplies basic information about a polymer, such as the band gap of the dissolved polymer determined using a UV/vis spectrometer, the molecular weight (M_W), and the oxidation/reduction levels of the polymer measured using cyclic voltammetry (CV).

At this point the researcher needs to learn how to produce uniform films of the new polymer mixed with the chosen fullerene without using too much of the valuable polymer. With the mixture of P3HT:PCBM, the PCE can increase tenfold with no change in layer thickness, concentration ratio, or deposition solvent [42]. This means that even if wise coating choices are made about the polymer solution and a highly uniform film is coated, the resulting PCE may still be much lower than that for an optimized morphology. The PCE increase for P3HT:PCBM comes from briefly annealing the film at 150°C, which causes a change in the nanoscale morphology and the altered morphology leads to an increase in PCE. The fabrication toolkit can therefore be further subdivided into fabrication steps that occur before, during, and after coating. The following sections attempt to describe the many interrelated but independently controlled fabrication parameters that affect morphology formation. We focus on how fabrication choices affect device morphology.

2.1.1 Molecular Weight

Unlike small molecules, polymers do not have a well-defined M_W and a polymer sample contains a distribution of molecular weights so it is difficult to compare the molar ratio with a small molecule such as C_{60} or PCBM. Instead, one typically reports a weight ratio or wt%, so the molar ratio of polymer repeat units with respect to PCBM is fixed. However, the polymer M_W has a large effect on the solubility of the polymer and the miscibility of the polymer with the fullerene. Smaller M_W polymers or oligomers are in general more soluble and so can be processed with a wider variety of solvents. However, the smaller M_W means that the polymer chains are less entangled and that all species in both solution and melt phases can diffuse more quickly. As a result, low M_W polymers and oligomers tend to make less viscous solutions, phase separate on a larger length scale, and low M_W films are more likely to de-wet or form voids.

The relationship between polymer M_W and PCE has been exhaustively studied in P3HT and mixtures with PCBM [49–61]. We will attempt to briefly summarize the lessons here. First, a lower M_W polymer is more soluble and more miscible with PCBM. Also, in pure P3HT samples, it has been shown that aggregated domain content (for a given solvent and temperature) increases with M_W up to ~20 kDa as a result of increased regioregularity and reduced sample entropy [54, 62]. Even higher M_W (~70 kDa) P3HT has been shown to form highly crystalline nanofibers that can be solution processed [63, 64]. In mixed samples, the PCBM interferes with the formation of pure P3HT domains, so the P3HT is less crystalline. The P3HT crystallinity can be reintroduced by annealing the sample to allow phase separation. For a high regioregularity and M_W, the solubility of PCBM in P3HT is ~30% [65].

Another important result was the realization that charge mobility did not necessarily scale with crystallinity [58]. Kline et al. and others showed that for pure P3HT, lower M_W polymer formed samples with higher apparent crystalline content but that the crystals had few connecting polymer strands leading to poor

macroscopic charge mobility due to a high activation barrier to charge hopping. In contrast, in high M_W P3HT the crystalline domains were well connected to adjoining crystalline domains by individual polymer chains, and so the activation barrier for charge hopping is much lower [54, 58]. A more detailed discussion of the morphology of P3HT thin films can be found in the chapter "Morphology of P3HT in Thin Films" by Kim Tremel and Sabine Ludwigs in this book [66]. Various studies have shown that a M_W of less than 20,000 kD is too low for high efficiency OPV devices [52, 54, 57]. High M_W P3HT is also undesirable because it requires higher boiling point solvents and longer equilibration times for morphology formation [52]. The "Goldilocks" region for M_W for P3HT used for OPV is 20,000–75,000 kD with a maximum possible regioregularity [67, 68].

2.1.2 Solvent Choice

The choice of casting solvents became a clear issue in 2001 when Shaheen et al. published an article showing a PCE increase from 1.1 to 2.5 % for MDMO-PPV:PCBM OPV devices cast from toluene and chlorobenzene, respectively [36]. Subsequent studies showed that toluene was a better solvent for the MDMO-PPV than PCBM, so the PCBM crystallized out of solution with large domain sizes (>1 μm) that reduced the device quality [69]. However, chlorobenzene and dichlorobenzene are equally good solvents for both polymer and fullerene so the polymer and fullerene remain miscible to higher concentrations and the resulting domain sizes are much smaller (tens of nanometers) [69].

A zero-order statement about solvent choice is that the solvent must be equally good for each component to avoid large-scale phase separation. The next thing to consider is the absolute solubility of the polymer and fullerene. Polythiophene and C_{60} have negligible solubility in any solvent, whereas P3HT and PCBM have side chains that greatly increase their solubility. Nevertheless, concentrations of at least 10 mg/mL are necessary to obtain highly planar films of >80 nm thickness without defects using spin-coating. In general, a higher solubility is desired so that more concentrated solutions can be made and a wider variety of coating techniques can be employed. P3HT and PCBM have shown the highest solubility in polar aromatic solvents such as chlorobenzene, 1,2 dichlorobenzene, and 1-chloronaphthalene.

Another important consideration is the boiling point (BP) of the solvents. The BP determines how quickly the solvent evaporates and thereby the formation rate for polymer and fullerene domains. Polymer domains that equilibrate slowly in high BP solvents tend to be more crystalline (thermodynamic product) whereas low BP solvents evaporate quickly and yield mixed amorphous films (kinetic product). When spin-coating at 1,000 rpm, a 20 mg/mL solution of 1:1 P3HT:PCBM condenses to a film in 1–3 s when processed with $CHCl_3$ (BP = 61°C), 5–10 s when processed in chlorobenzene (BP = 132°C), and the film remains wet after 60 s when processed with 1,2 dichlorobenzene (BP = 182°C) (Moulé, personal observation) [70]. The change in structural order in P3HT is observed in a red shift of the absorption spectrum and formation of a clearly defined vibronic structure [71]. The

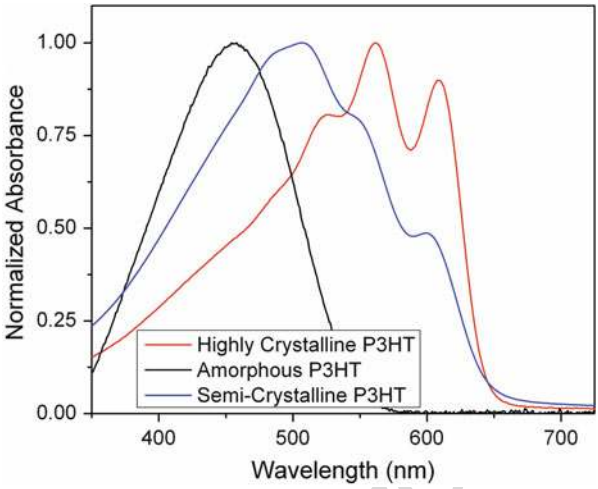

Fig. 4 Solution absorption spectra for P3HT dissolved in $CHCl_3$ (*black*) and anisole (*blue*), and for P3HT nanofibers slowly cooled, filtered, and re-dispersed into toluene (*red*) [63]

idea to increase crystallinity of the P3HT with slower solvent evaporation was used by Li. et al. to achieve the first record PCE over 4% for OPV [43].

With the introduction of semicrystalline polymers like P3HT, it became clear that the solvent could affect the formation of P3HT aggregated or crystalline structures in solution as well as in films. Figure 4 shows three liquid state UV/vis absorption spectra of P3HT dissolved in $CHCl_3$, anisole, and toluene, which result in the formation of ground state structures that are amorphous, somewhat crystalline H-aggregates, and highly crystalline J-aggregates, respectively [72]. The red shift of P3HT with increased order and (to the eye) very obvious color shift makes it an easy polymer to work with. Without any device measurement, one can look at the film and learn a lot about the nanoscopic order by observing the color.

2.1.3 Weight Ratio

The weight ratio between the donor polymer and acceptor fullerene in the final film has a large effect on the PCE of an OPV device. The ideal or correct weight ratio is usually defined as the ratio that achieves the highest PCE. However, there is a strong correlation between weight ratio, layer thickness, and domain size that makes clear that weight ratio, while easy to control, is not easily understood.

One highly useful generalization for OPV device function is that layers with matched hole and electron mobilities have higher FF and that devices with mismatched charge mobilities develop space-charge-limited current (SCLC) layers, particularly with increased light intensity [73]. We can clearly state that one reason to adjust the donor/acceptor weight ratio is to increase or decrease the relative mobilities of the hole and electron carrying materials [74]. One particular example of this relationship showed that for both P3HT:PCBM and OC_1C_{10}-PPV:PCBM, thicker layers perform better with increased PCBM content whereas thinner devices

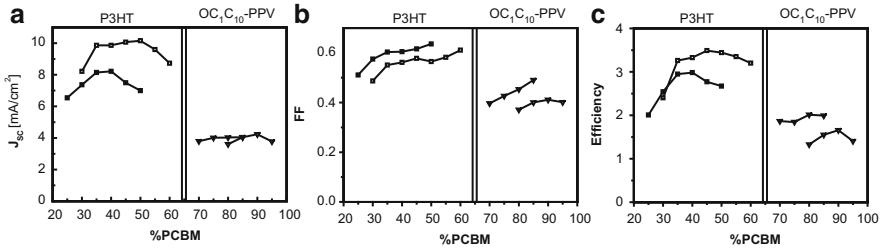

Fig. 5 (**a**) J_{sc}, (**b**) FF, and (**c**) PCE as a function of weight percentage of PCBM for P3HT:PCBM devices with thickness $L = 215$ nm (*open squares*) and $L = 105$ nm (*closed squares*), and for OC_1C_{10}-PPV:PCBM devices with $L = 190$ nm (*open triangles)* and $L = 80$ nm (*closed triangles*)

perform better with reduced PCBM (Fig. 5). The explanation is that the polymer absorbs more light than the fullerene in the visible range, so the absorption density and thereby J_{sc} is higher with increased polymer content. However, as the layer thickness increases, the FF is reduced because of the increased path length, which yields increased recombination and greater series resistance. An increased PCBM content in the layer balances the charge mobilities for thicker devices, yielding an increase in FF. For P3HT:PCBM, the total charge mobility is higher and well matched, so 200–400 nm OPV devices still function well [70]. In contrast, the hole mobility (μ_h) is 100 times lower in OC_1C_{10}-PPV than in P3HT, so balanced charge mobility is not possible for any device, and devices thicker than 100 nm suffer from greatly reduced FF [70].

Early in the OPV literature, it was common to publish a concentration and thickness dependence of the *J*/*V* characteristics for new polymer/fullerene mixtures [70, 75–81]. This information is very interesting, but ultimately was not as useful as desired because each group had slight differences in fabrication procedure and polymer batch that led to large differences in morphology and ultimately in PCE [82]. The difficulty in comparing samples between different research groups has led to a tendency for many groups to publish the "hero" efficiency result without properly reporting all of the fabrication steps necessary to repeat the result. This tendency to focus on PCE without reporting the details of fabrication has led to a great redundancy in OPV literature. We recommend that fabrication data still be published (even if only in the supplemental section) to reduce repeated studies. Accurately representing the data can be difficult. Figure 6 shows the optimization of BHJ layer thickness, and wt% PCBM with respect to PCE for a mixture of poly [4,4-bis(2-ethylhexyl)-4*H*-cyclopenta[2,1-b;3,4-b]dithiophene-2,6-diyl-alt-4,7-bis (2-thienyl)-(2,1,3-benzothiadiazole)-5′,5″-diyl] (PCPDTTBTT) with PCBM [83]. The color of the points indicates different solvents. The complexity (difficult readability) of this plot is meant to show that it is difficult to display fabrication information in a sufficiently dense format. Tables are popular but often fail to present the trend in the data. Nevertheless, publishing detailed fabrication information will reduce redundancy and confusion in the literature.

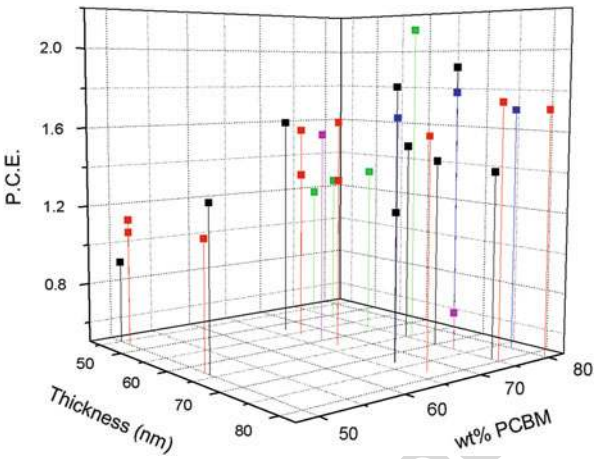

Fig. 6 Optimization of PCE data with respect to BHJ layer thickness, wt% PCBM, and casting solvent for a mixture of PCDTTBTT with PCBM. The *colors* indicate different solvents: chlorobenzene (*black*), *o*-xylene (*red*), chlorobenzene + anisole (*green*), *o*-xylene + anisol (*blue*), and chlorobenzene + nitrobenzene (*magenta*) [83]

2.1.4 BHJ Layer Thickness

As indicated in the two plots in Fig. 6, the BHJ layer thickness and PCBM concentration ratio are not independently optimized fabrication parameters. This is because an increase in the BHJ layer thickness increases both the total light absorbance and the transport distance to the electrode. Several articles and reviews describe how light absorbance into BHJ layers increases nonlinearly as a result of interference between incident and reflected radiation [8, 84–86]. This interference pattern means that more light is absorbed into a BHJ layer that is 70–100 nm thick than into a layer that is 120–150 nm thick. Peumans et al. pointed out that constructive interference is maximized in a BHJ layer with thickness near $\lambda/4n$ and minimized at a thickness near $\lambda/2n$, where n is the refractive index of the active layer. Peaks in simulated sunlight absorbance occur at 80, 210, and 330 nm for a thermally annealed mixture of 1:1 P3HT:PCBM and at 110 and 230 nm for a solvent-annealed 1:1 P3HT:PCBM device [84, 85]. There are differences between thermally annealed and solvent-annealed samples in both the internal morphology [87, 88] and thermally induced mixing between the BHJ layer and poly(3,4-ethylenedioxythiophene):poly(styrene sulfonate) (PEDOT:PSS) [85, 89]. When PSS mixes with P3HT, the P3HT is oxidized and bleaches, which reduces the effective thickness of the active layer [85, 89].

Figure 7 shows J_{sc}, FF, and PCE for P3HT:PCBM and OC_1C_{10}-PPV:PCBM devices as a function of layer thickness [70]. Both device types show a peak–dip–peak in J_{sc} with increasing layer thickness. However, the first peak (~70 nm) in the J_{sc} of OC_1C_{10}-PPV:PCBM devices is much higher than the second peak, indicating that the electrical quality of the layer decreases with increasing thickness. As indicated above, the charge carrier mobilities in the hole-carrying and electron-carrying domains must be matched for high J_{sc} or PCE. Because the μ_h of OC_1C_{10}-PPV is much lower than μ_e of PCBM, this device type builds up a space charge layer and thicker devices show reduced performance. In contrast, the thicker

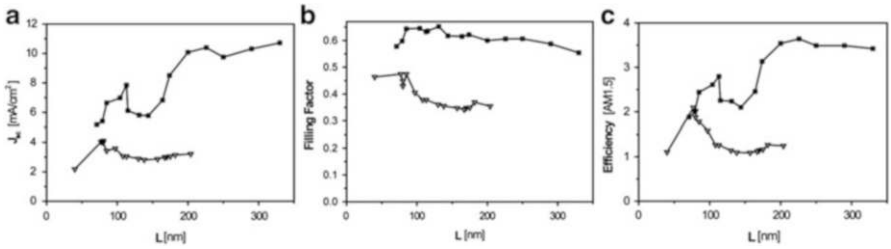

Fig. 7 Thickness dependence of (**a**) J_{sc}, (**b**) FF, and (**c**) PCE for 1:1 P3HT:PCBM (*squares*) and 1:4 OC_1C_{10}-PPV:PCBM (*triangles*) OPV devices illuminated by AM1.5 source at 100 mW/cm^2 intensity [70]

~210 nm P3HT devices have higher J_{sc} and PCE than devices with lower thickness. P3HT is able to make good thicker devices with PCBM because the μ_h of P3HT and μ_e of PCBM are comparable [74, 90].

Comparison of the peaks in J_{sc} between devices based on P3HT and OC_1C_{10}-PPV shows a second systematic difference. The PCE maxima shown in Fig. 7 for OC_1C_{10}-PPV devices are at ~70 and ~190 nm, whereas for P3HT-based devices the maxima occur at 110 and 230 nm. This shift in the position of the maxima comes because P3HT absorbs a red-shifted radiation compared to OC_1C_{10}-PPV (band gap = 1.9 eV rather than 2.2 eV). Because low energy photons have a longer wavelength, the interference pattern selects for maximum absorbance at a greater thickness than for higher energy photons [84].

2.2 The Post-deposition Toolkit

2.2.1 Solvent Annealing

Solvent-coating is a process whereby external forces are used to deliver a thin, uniform wet film. Spin-coating produces wet films by wicking excess solution off the substrate using centrifugal forces. Figure 8 shows a plot of wet layer thickness versus spinning time at 1,500 rpm for a 2:1 mixture of P3HT:PCBM in a chlorobenzene solvent [91]. Formation of the initial wet film and wicking of excess solution occurs in the first step (Fig. 8, step a). The wet film contains all of the polymer that will be in the final film plus solvent. The wet film (Fig. 8, step b) thins rapidly due to evaporation of the solvent and collapses to the final dry thickness after ~6 s (Fig. 8, step c) (note that the time of ~10 s mentioned in Sect. 2.1.2 corresponds to a lower spinning speed). The final stage is evaporation of solvent from the collapsed film (Fig. 8, step d). The order of the polymer as measured using GIWAXS and GISAXS shows that crystal ordering occurs slowly in the wet film and that domain sizes form quickly during solidification.

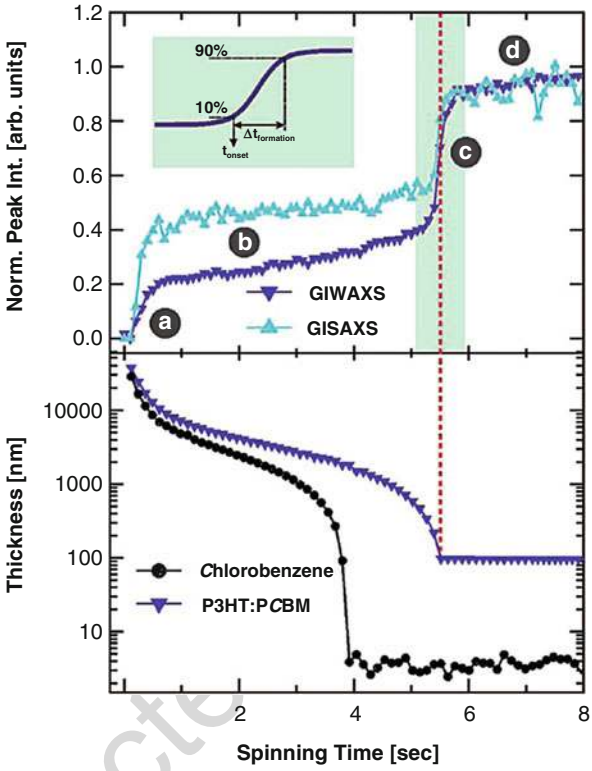

Fig. 8 Quantitative timeline of the spin-coating process of a P3HT:PCBM blended solution. The *upper graph* shows the normalized crystallization and aggregation peak intensities as a function of the spinning time during the spin-coating of P3HT:PCBM (62.5:37.5 wt%). The *light green box* indicates the time range where crystallization and phase separation occur. The onset of film formation t_{onset} and its duration $\Delta t_{formation}$ are defined in the *green inset*. The *lower graph* shows the thickness versus time during the spin-coating process of the pure solvent and the P3HT:PCBM solution, respectively. Reprinted (adapted) with permission from [91]. Copyright © 2013 Wiley-VCH Verlag GmbH & Co. KGaA, Weinheim

AU7

As discussed above, high BP solvents evaporate slowly (10 s–10 h), leaving the polymer a long time to relax into unstrained and, depending on the polymer, crystalline domains. In contrast, low BP solvents evaporate quickly (<10 s), leaving the polymer in an amorphous form with strain that can cause dewetting.

In the OPV field, the drying time for a film was not purposefully controlled until solvent annealing experiments were published by the Yang group in 2005 [43]. The process of solvent annealing involves covering the wet film (with a petri dish or other cover), which keeps the atmosphere above the sample rich in solvent and prevents evaporation. In this way, the sample can be allowed to relax over hours instead of seconds [88, 92]. Solvent annealing for OPV blends has been widely reported. The Yang group also showed that the solvent annealing effect could be realized with any solvent if a high solvent partial pressure above the sample could be maintained [92]. A simple method for doing this is to spin-coat a wet film and then to cover the wet film and substrate with an up-turned petri dish. Assuming negligible mass transfer of solvent to outside of the petri dish, the film remains solvent-swollen for an arbitrary time period. Several review articles have detailed the change in morphology with solvent annealing [87, 88, 92]. In general, the longer relaxation times afforded by high boiling point solvents leads to increased crystallinity in P3HT films [88]. The crystallization of P3HT forces PCBM out into a

mixed amorphous P3HT:PCBM phase [93]. With increased PCBM density, the PCBM also starts to form pure amorphous and crystalline domains [94, 95]. Solvent annealing causes greater phase separation between P3HT and PCBM than thermal annealing [96].

2.2.2 Thermal Annealing

A more commonly used method for causing phase separation between P3HT and PCBM is thermal annealing. Thermal annealing of P3HT and mixtures of P3HT with PCBM has been studied in great detail [42, 56, 59, 70, 76, 97–117]. Optimized thermally annealed devices are spin-coated from a chlorobenzene solution in a ratio that contains 35–45% PCBM by weight. After spin-coating, the metal electrode is evaporated and then the device is heated for 5–30 min at ~150°C [42]. PCE as high as 5% for this device type have been reported [42] but 3.5–4.5% PCE is more common.

Moulé and Meerholz published two articles that described measurement of EQE as a function of BHJ layer thickness. Several thousand individual P3HT:PCBM OPV devices were fabricated to establish these data sets [70, 85]. We found that OPV devices with PCE of ~4% could regularly and repeatably be fabricated using the thermal annealing method with BHJ thicknesses of 80–350 nm. The solvent annealing method occasionally brought "hero" devices, but in general was less easy to control because the trace solvent atmosphere in the glove-box had a large effect on the final morphology [118]. During the fabrication of so many devices we found three issues that were likely to reduce device quality (without changing substrates or metal type):

1. Occasionally, there is a PEDOT:PSS batch supplied that produces exclusively S-shaped *J*/*V* curves with low FF [119, 120] This problem could only be solved by ordering new PEDOT:PSS and is attributed to slight changes in the doping level of the PEDOT:PSS itself.
2. The quality of P3HT varies widely between batches, which mostly has an effect on the FF. Average FF > 0.6 is an indication of "good" P3HT. Typically, a graduate student can achieve "good" results with a year of practice and with ~50% of the P3HT batches received. Cleaning the P3HT by dissolving and then dripping into a solution of CH_3OH:H_2O improves the FF by an average of 0.05. The improvement most probably comes from the removal of metals.
3. We have also informally found that evaporation of metal electrodes at a high rate can reduce the FF because the hot metal damages the polymer. We use an initial evaporation rate of 0.02 nm s^{-1}.

Two different two-component nonequilibrium phase diagrams have been made for P3HT:PCBM [121, 122]. Figure 9 shows the expected phase behavior of P3HT:PCBM in a melt or solidifying melt [121]. Thermal analysis is able to show the mixing ratio of P3HT:PCBM as a function of temperature. All investigations agree that PCBM has ~30% miscibility with P3HT and that with higher PCBM content,

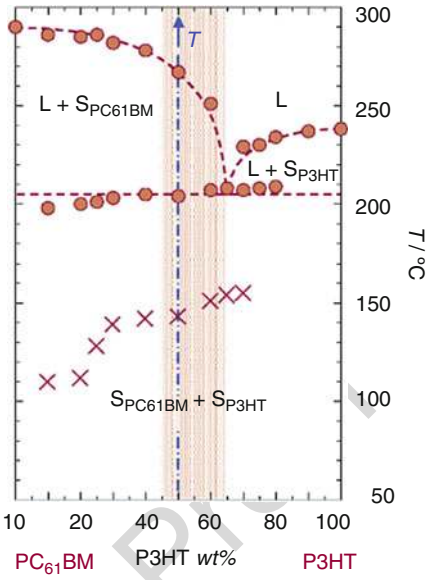

Fig. 9 Two component nonequilibrium phase diagram for P3HT:PCBM measured using differential scanning calorimetry. Reprinted (adapted) with permission from [121]. Copyright © 2008 WILEY-VCH Verlag GmbH & Co. KGaA, Weinheim

phase separation occurs. In addition, it has been widely reported that with heating, PCBM diffuses through the P3HT and forms extended crystals that are detrimental to OPV device function [118, 121, 123–125]. Some recent attempts have been made to generate fullerenes that do not crystallize in order to improve the device longevity [126].

Although thermal analysis can show the mixing ratio of P3HT:PCBM in a volume and the melting temperatures of crystals in the melt, it does not specify the miscibility between the amorphous P3HT and PCBM. Recent bilayer device investigations [127], neutron reflectometry [65, 128, 129], soft X-ray spectroscopy [95, 125], and 3D electron tomography images of P3HT:fullerene [96] have revealed that a mixed domain always exists between P3HT-rich and fullerene-rich domains. This means that P3HT:PCBM forms four separate domain types: P3HT and PCBM can each crystallize to form pure domains, P3HT and PCBM mix in a ~3:7 ratio in a mixed amorphous P3HT:PCBM domain, and amorphous PCBM with ~10% amorphous P3HT is also commonly found [130]. Spin-coating results in the rapid formation of a film and the most common phase is the mixed 3:7 amorphous domain type. With either solvent annealing or a short period of thermal annealing, the mixed domain phase separates into pure P3HT domains and amorphous PCBM domains with low P3HT content. With thermal annealing for longer times, PCBM seed crystals form and Oswald ripening occurs, which leads to increasingly large pure PCBM domains. Large PCBM domains result in a reduction of OPV device quality.

2.2.3 Co-solvent Additives

Examining solvent and thermal annealing as industrial processes showed that there were clear disadvantages to both post-deposition annealing methods. Solvent annealing utilizes long times with partially solvent-swollen films to allow the morphology to develop towards a more equilibrium-like configuration. By more equilibrium-like we mean a more crystalline, more phase-separated, and more relaxed structure. However, long annealing times and long solvent removal times are incompatible with rapid reel-to-reel coating.

There are also disadvantages to thermal annealing as a process in OPV manufacture. Thermal annealing also allows the BHJ layer morphology to develop towards a more equilibrium-like configuration. However, because the whole substrate must be heated, there is a possibility that other layers are affected. For example, it was shown that with heating to 150°C, P3HT reacts with PEDOT:PSS to make a mixed doped layer via the following reaction [89]:

$$2\text{P3HT} + 2\text{PEDOT} : \text{PSS} + \Delta \rightarrow 2\text{P3HT}^{+}\text{PEDOT} : \text{PSS}^{-} + \text{H}_2$$

Also, heating to elevated temperatures increases the diffusion rate of PCBM in P3HT, which leads to the formation of extended PCBM crystals and reduced device quality [102, 118, 131–134].

Given these considerations, it was clear that another method for the development of OPV morphology needed to be invented. In 2006, Zhang et al. published an article showing that if mixed solvents are used as a casting solution, the higher BP solvent would remain in the film longer and the film morphology would develop as if the entire solvent was the higher BP solvent [135]. This result gave rise to several useful ideas. First, halogenated solvents have always been an issue for scale-up of OPV because laws governing their release to the atmosphere are quite strict. It would be much less expensive if non-halogenated solvents could be used or if much smaller quantities of halogenated solvents could be used [50, 136]. Second, if high BP solvent-additives can be used to better solubilize both the donor and acceptor components, a different additive could be used that selectively affects one component or the other. Peet et al. published the use of a solvent additive that selectively solvated PCBM while acting as a nonsolvent for the donor polymer [44]. In subsequent research that compared several PCBM selective additives, it was determined that 1,8-di-iodo-octane (DIO) produced BHJ layers with the highest PCE [137]. Moulé et al. published the use of nitrobenzene (NB) as a nonsolvent additive for both P3HT and PCBM [45]. Both DIO and NB produce unannealed P3HT:PCBM devices with PCE near 4% [45, 138]. DIO has been shown to be an essential solvent additive for many copolymer donors in mixtures with PCBM and $PC_{71}BM$.

A solvent additive for OPV can be either a good solvent, selective solvent, or a nonsolvent for both species. The solvent additive must have a higher BP than the carrier solvent so that as the carrier solvent evaporates off, the co-solvent additive concentration increases. This means that the wet film thickness and concentration is created with the main solvent, but the morphology forms under the thermodynamic

conditions established by the co-solvent. DIO is by far the most popular co-solvent in terms of citation frequency. It has been used with most of the new low band gap alternating push–pull copolymers and often yields a superior PCE than films cast without DIO.

2.2.4 Pre-formed Polymer Particles

A further fabrication technique that has been used for OPV devices is the use of preformed polymer nanoparticles. Berson et al. published an article that examined the formation of P3HT nanofibers in solution, followed by coating the nanofibers with PCBM to form a BHJ layer [64, 139]. The idea behind the experiment was that highly crystalline P3HT fibers could be formed in solution that would have fewer defects than P3HT domains in a typical BHJ film. The principle is correct and the spectrum of P3HT fibers shows considerably more vibronic character than P3HT films [64, 139]. Subsequent work on P3HT fibers showed that P3HT forms highly fluorescent J-aggregates in solution under slow cooling conditions [63, 72, 140]. However, OPV devices cast from P3HT fibers have lower PCE than normal BHJ devices of the same thickness [64, 141]. It is known that the P3HT fibers lie within the plane of the film, so it is possible that the fibers are poor conductors of holes. In this case, we expect the J_{sc} to be lower due to increased recombination at unattached fibers. Also, the FF is expected to be lower because it probably requires an activation potential for a hole to hop from one fiber to the next. This activation barrier would appear as a series resistance and reduce the FF.

The mechanism was tested by adding a small amount of amorphous P3HT to the P3HT fibers and re-fabricating OPV devices [64]. The OPV devices with some amorphous P3HT had increased J_{sc} and FF. The authors concluded that the P3HT fibers lacked connectivity and that addition of some amorphous P3HT reestablished the connectivity between P3HT domains [64]. Several other thiophenes were tested for polymer nanoparticle-based OPV devices. It was found that poly (quaterthiophene) (PQ12T) was too insoluble and that polymer domains with extended sizes formed in solution [141]. Oosterbaan et al. fabricated nanofibers from a series of thiophenes with side chain length from 3 to 9 [139]. They concluded that P3HT has the ideal side chain length for polymer nanofiber OPV. Shorter side chains leave a less-soluble polymer that is immiscible with PCBM so OPV device layers do not have enough donor–acceptor interface, which reduces the charge separation probability. Longer side chains destabilize the polymer fibers and allow defects within the fiber to form. For long side chains, the miscibility with PCBM is too high and too much intermixed donor–acceptor phase forms, leading to increased recombination [139]. Another study of polymer nanofiber OPV was published by Xin et al., who worked on characterization of P3BT:$PC_{71}BM$ nanofiber OPV devices (Fig. 10) [142]. P3BT:$PC_{71}BM$ formed OPV devices with high EQE and increased efficiency compared with the Oosterbaan study. Analysis of the fabrication method shows that a combination of nanofiber formation (solvent

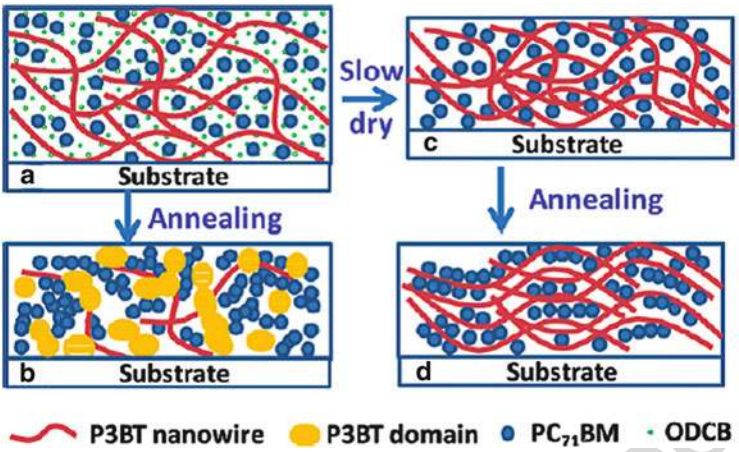

Fig. 10 Solvent annealing followed by thermal annealing yields a morphology for P3BT:$PC_{71}BM$ that cannot be reached by another fabrication pathway. Reprinted (adapted) with permission from [142]. Copyright 2010 American Chemical Society

annealing) and thermal annealing was used to create the optimized morphology film [142].

All of the experiments described above were designed to create more crystalline P3HT domains, and the domain size was controlled by the self-assembly of the P3HT fibers. An alternative need is to control the domain size between two noncrystalline polymers. In this case, the domain size can be set by fabricating polymer nanoparticles in solution [143]. One strategy for fabrication of mixed polymer nanoparticles is shown in Fig. 11. Here the polymer concentration, surfactant concentration, and surfactant strength all affect the size of the final polymer domain [143].

3 Optical Properties

One remarkable feature of solid P3HT:PCBM blends is that their optical properties depend largely on the preparation conditions [73, 144, 145]. Because absorption and emission spectra are easier to record than, for example, X-ray scans and TEM images, the quantitative analysis of optical data with regard to morphology is of great interest. Figure 12 shows exemplary optical absorption spectra of as-prepared and annealed P3HT:PCBM measured at room temperature, together with the corresponding *J*/*V* device characteristics. Here, the films were cast from chloroform, a low-boiling point solvent, and were annealed at the given temperatures for 10 min each. With annealing at higher temperatures, the long wavelength features at 560 and 610 nm attributed to absorption of planarized P3HT chains in polymer

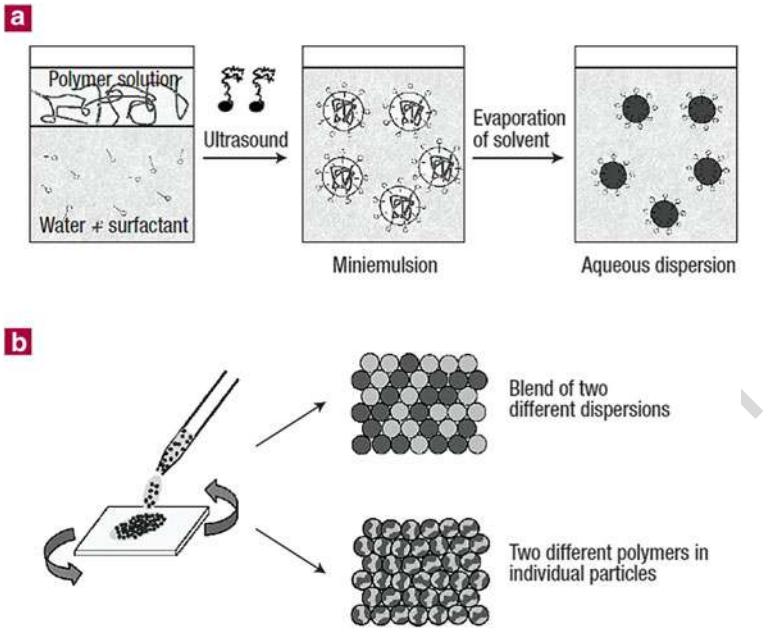

Fig. 11 (**a**) Preparation of a dispersion of solid polymer nanoparticles in water. First, a solution of the polymer in an organic solvent is mixed with water containing an appropriate surfactant. A miniemulsion is then formed upon stirring and ultrasonication. Finally, the solvent is evaporated, resulting in solid polymer nanoparticles dispersed in water. (**b**) Strategies for preparation of binary polymer blends using polymer nanospheres. Phase-separated structures at the nanometer scale can be prepared either by coating a layer from a dispersion containing nanoparticles of two different polymers, or by using dispersions that contain both polymers in each individual nanoparticle [143]

crystallites become more prominent. At the same time, the short-circuit current and the fill factor of the device both increase continuously.

A recent model by Spano enables a quantitative analysis of regioregular P3HT absorption spectra in relation to the morphology [147, 148]. This model was developed to describe the absorption of and the emission from H-aggregates comprising parallel-aligned cofacially packed conjugated chains in the case of weak exciton coupling. In this limit, the splitting of the electronic levels due to Coulombic interactions is considerably smaller than the vibrational energy. As a result, interchain coupling leads to the formation of vibronic bands with their width essentially determined by the exciton bandwidth W. It was shown later that W is inversely related to the length of the interacting chain segments in a P3HT aggregate [149]. An important prediction of Spano's model is that the exciton bandwidth affects the relative intensities of the individual transitions of the vibronic progression in the absorption. Clark et al. successfully applied this model to optical spectra of pure P3HT films with a variation in the solvent type used. Higher solvent boiling points led to smaller W values, which was attributed to an increase in the P3HT aggregate size [71, 150].

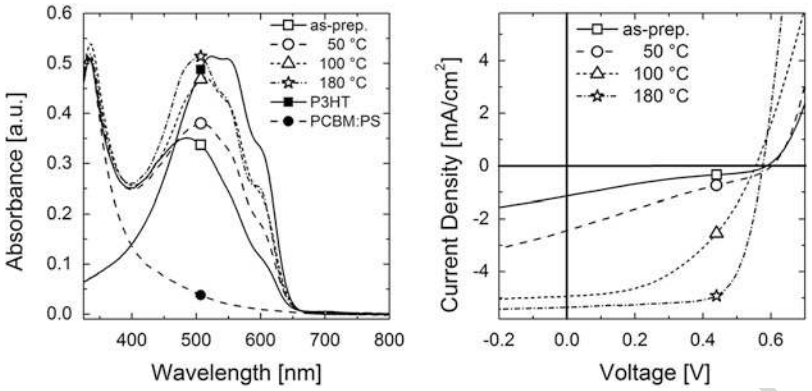

Fig. 12 Optical absorption spectra of P3HT:PCBM photoactive layers and the corresponding *J*/*V* characteristics of solar cells prepared with the same photoactive layer. The as-prepared film is the condition directly after spin-coating. The given annealing temperatures were applied for 10 min each, directly from the state after spin-coating. Also shown are the absorption spectra of a film of pure P3HT and a film comprising PCBM:PS, where the latter was used to determine the PCBM contribution to the P3HT:PCBM absorption spectra [146]. The active layer thickness was only 100 nm, which causes less absorption in the active layer and a lower photocurrent compared with optimized devices

This model has been successfully applied to understand the morphological changes of the P3HT phase in a 50:50 wt% P3HT:PCBM blend, where information about the crystallinity and interchain ordering of the polymer phase was determined [146]. A low and a high boiling point solvent were investigated with the use of different annealing temperatures. The absorption spectra analysis was compared with the solar cell performance in devices with identical active layers (Fig. 13). The low boiling point solvent, chloroform, led to a non-optimized initial film morphology. Compared to the as-prepared blend prepared from the high boiling point solvent dichlorobenzene, the chloroform-cast layer exhibited smaller aggregates, a lower degree of crystallinity, and a larger absorption bandwidth. Upon annealing, the degree of crystallinity of the P3HT component increased up to a temperature of ca. 70°C, with a correlated increase in the aggregate width from ca. 7 to 10 nm. The glass transition of a 1:1 blend of P3HT:PCBM has been observed to range from ca. 10 to 70°C [151–153]. It has, therefore, been concluded that annealing above the glass transition provides the chains with sufficient mobility to allow for the growth of existing polymer crystallites. Beyond the glass transition range, annealing had a surprisingly weak effect on the further changes to the degree of crystallinity. Neither the percentage of aggregated P3HT chains nor the aggregate width of annealed chloroform-cast layers reached the same level as found in the pristine P3HT layer cast from chloroform or as found in any of the dichlorobenzene-cast blends. It is plausible to assume that a further growth of P3HT crystallites in the chloroform-cast layers upon annealing at higher temperatures is prevented by an already-existing network of agglomerated PCBM molecules [154]. The Gaussian line width σ in the absorption spectra, however, decreased throughout the entire

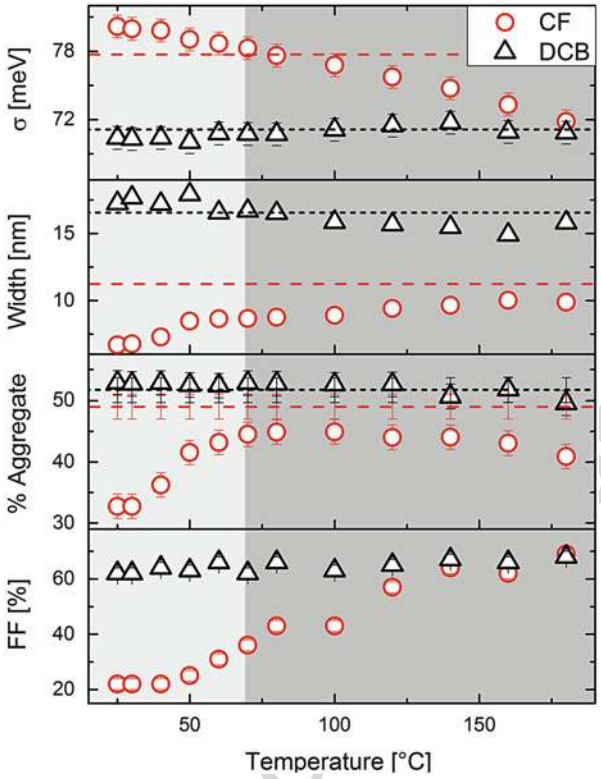

Fig. 13 Best-fit parameter of the aggregate P3HT component in the absorption spectra of P3HT:PCBM blends coated from chloroform (CF) and dichlorobenzene (DCB), with subsequent thermal annealing of the as-prepared film for 10 min at the indicated temperature. σ the Gaussian line width, *Width* aggregate width of the P3HT crystalline component, *% Aggregate* crystalline percentage of the P3HT component versus the total amount of P3HT, *FF* fill factor of the photovoltaic device with the same photoactive layer used in the optical absorption investigation. *Red* and *black dashed lines* show corresponding values measured on as-prepared layers of pristine P3HT, cast from CF and from DCB, respectively. The glass transition of P3HT:PCBM is shown by the change from *light* to *dark grey* background, with a glass transition temperature of around 60–70 °C [146]

range of annealing temperatures used. This decrease in the absorption line width is indicative that the intra- and/or interchain disorder is reduced. It was then shown that the decrease in σ goes along with a prominent increase in the hole mobility, enabling more rapid extraction of the photogenerated charges to the electrodes. As a consequence, non-geminate recombination becomes less efficient for higher annealing temperatures, which revealed itself in a prominent increase in the fill factor. As an important conclusion, we find that consideration of only the percentage of crystallinity and/or of the aggregate size is not sufficient to explain the overall effect of annealing on device properties.

Nevertheless, as efficient hole transport necessitates the existence of a percolation pathway of crystalline P3HT throughout the entire layer, knowledge about the degree of crystallinity and also about the 3D distribution of the different phases forming the P3HT:fullerene blend are highly important. A well-established method for obtaining information on these properties is electron tomography (ET) [79, 96, 155]. For example, Loos and coworkers applied ET to determine the amount and distribution of the crystalline P3HT component in P3HT:PCBM blends [79]. These samples were investigated directly after spin-coating or after thermal annealing for 20 min at 130°C. The overall degree of crystallinity (DoC) in the annealed samples was between 40 and 55%, depending on layer thickness. The DoC from ET compares nicely with the range of values given in Fig. 13 for annealed blends. Notably, ET on thin layers (50–100 nm) revealed an enrichment of the crystalline P3HT content close to the bottom side where hole extraction occurs [79]. On the other hand, 200 nm thick layers had a homogeneous distribution of P3HT crystallites, which is highly beneficial for the efficient collection of holes throughout the entire active blend.

Raman spectroscopy is another successful optical technique for study of the degree of molecular ordering in the P3HT phase of the P3HT:PCBM blend. The in-plane skeleton Raman modes of C=C and C–C stretching were studied by Tsoi et al. under excitation wavelengths ranging from resonant to nonresonant [156]. Although direct electronic excitations in the resonant range could lead to a strong fluorescent background that can cover Raman signals, this is still an important measurement technique because the resonant conditions provide information about the molecular structure. In order to better understand the changes in the morphology of the P3HT component, Raman spectra of regiorandom and regioregular P3HT were compared where the regioregular polymer is known to have a higher degree of ordering. These results were then compared with the Raman spectra from a blend of regioregular P3HT with PCBM. The C=C stretching mode was found to be the superposition of the ordered and disordered P3HT characteristics and this was used to quantitatively estimate the degree of molecular ordering in the blend. The degree of molecular ordering in the nonannealed blend compared with the annealed blend was found to increase from 42 to 94%, relative to the ordering of pristine regioregular P3HT. The percentage of crystallinity can then be estimated based on a known percentage of crystallinity in the pristine P3HT. Tsoi et al. assumes a crystallinity in the regioregular P3HT of 15% and hence a percentage crystallinity of 6 and 14% in the P3HT phase of the annealed and nonannealed blends, respectively. However, optical spectroscopy on pristine P3HT layers consistently showed a degree of chain aggregation of approximately 40–50% [62, 150], and even higher degrees of crystallinity were reported in bulk samples [157]. Using 50% as a reference value, the degree of aggregation as estimated from the Raman spectra is 21 and 47% in the nonannealed and annealed blends, respectively. This approximation seems to be more reliable, based on the results of previous studies. Therefore, with an accurate method for determining the percentage crystallinity in the pristine regioregular P3HT, the analysis of Raman

spectra provides a simple way to determine the percentage crystallinity in the P3HT:PCBM blend films.

In conclusion, optical spectroscopy is capable of quantifying some important morphological parameters of P3HT:PCBM blends. Annealing clearly enlarges the P3HT crystallites in the composites, but also improves intra- and interchain order within the polymer domains. It is documented that this improvement assists charge extraction via a higher hole mobility. Structural disorder was recently proposed to be one origin of gap states in semicrystalline polymer domains [158]. Although as-prepared chloroform-cast layers are less crystalline, they contain a noticeable number of aggregated chains. It has been postulated that free carrier generation in P3HT:PCBM cells is assisted by the delocalization of holes on fully conjugated chains [159]. It is, therefore, concluded that the number of aggregated P3HT chains in as-prepared blends is sufficiently high for the efficient photogeneration of free carriers (as documented in the next section), while the poor structural order in these layers prevents the efficient extraction of free carriers to the external circuit [146].

4 Geminate and Non-geminate Recombination

As described in the previous section, optimized samples of P3HT:PCBM exhibit high fill factors, meaning that the photogenerated current is independent of bias over a wide range. On the other hand, samples with non-optimum morphology suffer from low fill factors. In this case, the photocurrent becomes continuously smaller with increasing bias (decreasing internal electric field), which points to photocurrent losses that are most prominent at low internal electric field. Clearly, the identification of these loss processes in relation to morphology is of interest, not only with regard to an overall understanding of these complex devices but particularly when targeting the knowledge-based optimization of BHJ devices.

The elementary steps that lead to charge generation and extraction in BHJ solar cells are shown in Fig. 14. Free carrier formation from photogenerated excitons (created in either the donor or acceptor phase) involves formation and split-up of interfacial electron hole pairs (often called geminate pairs because they origin from the same photoexcited exciton). As these pairs can be generated directly via optical sub-bandgap excitation, they are commonly denoted as charge transfer states. Geminate pairs may either split up into free carriers or recombine geminately to the ground state. Clearly, the competition between these two processes sets the upper limit for the efficiency of the internal photon-to-charge conversion. The second important step is the extraction of photogenerated charge to the electrodes. The efficiency of this process is, in general, not unity because these charges might recombine with carriers of opposite sign (either free or trapped, photogenerated or injected) on their way to the electrodes. This recombination is called “non-geminate” or “free carrier recombination”. Therefore, the efficiency of an organic donor/acceptor blend is determined by the fate of three elementary states (see Fig. 15): the photogenerated exciton (mostly singlet excitons) with energy E_{S1}, the charge

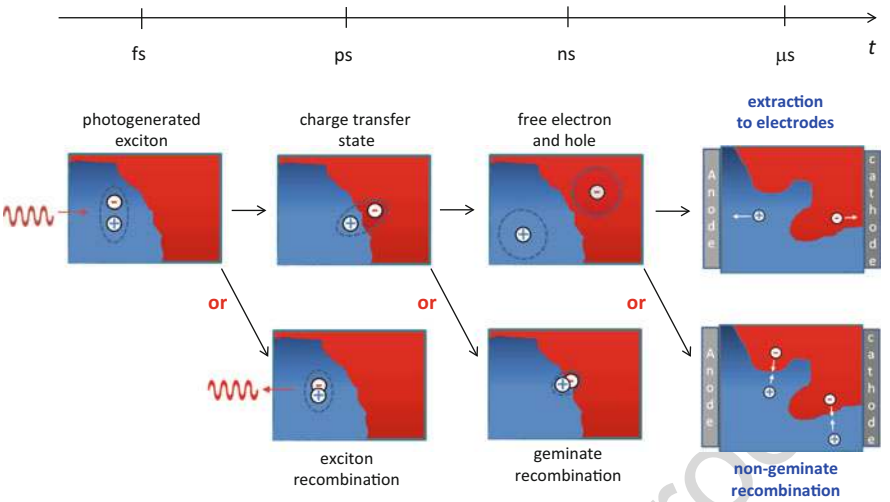

Fig. 14 Processes leading to free carrier generation and extraction. Absorption of light leads to the generation of a tightly bound intramolecular exciton (in P3HT:PCBM, the absorption in the visible spectrum is dominated by the polymer). This exciton decays to the ground state within its fluorescence lifetime or it diffuses to the donor–acceptor heterojunction where it dissociates into an interfacial electron–hole pair (charge transfer state). Due to the low permittivity of organic media, the interfacial polaron pair is bound by its mutual Coulomb potential. The charges forming this pair either overcome this potential to form free carriers, or they recombine geminately. Then, the free electron and the hole become extracted at the electrodes or they recombine non-geminately with other charges. The time scale for exciton dissociation, free carrier formation, and charge extraction is plotted at the *top*. Numbers should be taken with care because the charge carrier dynamics in blends depends very much on the chemical structure and morphology of the donor–acceptor mixture

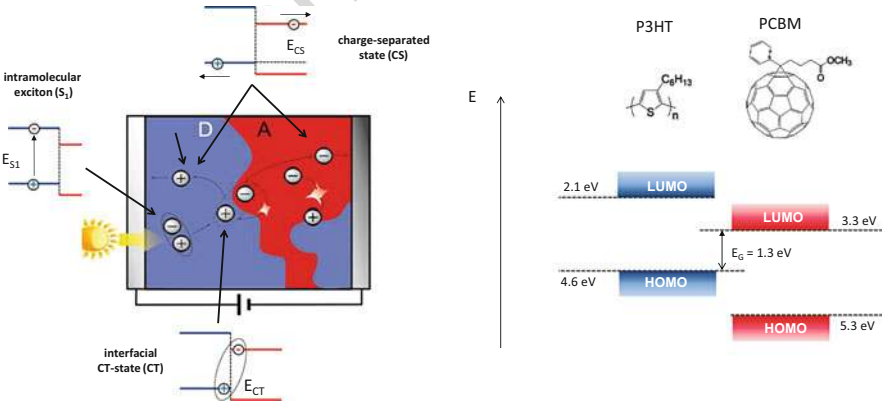

Fig. 15 *Left*: Donor–acceptor bulk heterojunction device and the relevant elementary states. *Right*: HOMO and LUMO energies of P3HT and PCBM in the 1:1 blend as determined by photoelectron spectroscopy (values taken from [160])

Table 1 Energies of the relevant states and excitations in blends of P3HT with PCBM

Blend	Energy (eV)	Reference
P3HT LUMO[a,b]	2.13	[160]
P3HT HOMO[a,b]	4.65	[160]
$PC_{61}BM$ LUMO[a,c]	3.80	[160]
$PC_{61}BM$ HOMO[a,c]	5.80	[160]
P3HT:$PC_{61}BM$ LUMO[a,d]	3.29	[160]
P3HT:$PC_{61}BM$ HOMO[a,d]	4.63	[160]
P3HT:$PC_{61}BM$ charge separated state[e]	1.34	
P3HT absorption onset[f]	1.68	
$PC_{61}BM$ absorption onset[f]	1.61	
Charge transfer state[g]	1.14	[161]

[a]Measured by photoelectron spectroscopy (PES) and inverse photoelectron spectroscopy (IPES)
[b]Pure P3HT layer, coated from chlorobenzene on either Si or Au
[c]Pure $PC_{61}BM$ layer, coated from chlorobenzene on either Si or Au
[d]P3HT:$PC_{61}BM$ (1:1) blend coated from chlorobenzene on Au, once buried interface. Similar values are seen for as-prepared and annealed samples
[e]Calculated from the P3HT:$PC_{61}BM$ (1:1) HOMO and LUMO energies given in the rows above
[f]From the extrapolation of the absorption onsets of the pure materials in Fig. 18b
[g]P3HT:$PC_{61}BM$ (1:1) on PEDOT:PSS, room temperature

transfer (CT) state with energy E_{CT}, and the charge separated (CS) state with energy E_{CS}. The CS state is different from the CT state in having overcome any mutual electron–hole interactions.

Because of the low dielectric constant of organic materials, the interfacial electron–hole pair is bound by Coulombic forces. Consequently, the energy of the CT state is expected to be smaller than that of the free electron–hole pair $E_{CT} < E_{CS}$. On the other hand, efficient photon-to-electron conversion is energetically favored only if the energy of the primary excitation is larger than that of the final product, meaning that $E_{S1} > E_{CS}$. Energies of the relevant species are listed in Table 1 for P3HT:PCBM. HOMO and LUMO energies in the blend are depicted in Fig. 15. The energy of the charge separated state was taken as the difference between the P3HT HOMO and the PCBM LUMO in the blend. The values suggest that the CT state has indeed the lowest energy, meaning that its split-up into free carriers is hampered by a potential barrier. However, note that the simple energy scheme drawn in Fig. 15 does not account for the heterogeneity of the P3HT:PCBM blend films, which has a large impact on the photovoltaic performance (see next section).

4.1 Free Carrier Generation Versus Geminate Recombination

A well-established model to describe free charge generation in isotropic media via split-up of Coulombically bound geminate pairs is the Braun–Onsager theory [164] (see also [165] for a detailed discussion on the accuracy of the model). Carriers are

considered to be free if their distance exceeds the Coulomb capture radius, meaning that the thermal energy is larger than the mutual Coulombic binding energy of the geminate pair. Free carrier formation involves a Brownian-type random walk that is well described by the Onsager theory. In general, the photogeneration efficiency P is a function of both the internal electric field and temperature:

$$P(E,T) = \frac{k_{\mathrm{d}}(E,T)}{k_{\mathrm{d}}(T,E) + k_{\mathrm{f}}}, \tag{6}$$

where k_{d} is the field- and temperature-dependent rate for charge separation and k_{f} is the inverse lifetime of the bound e–h pair. Although the Braun–Onsager model was originally developed for homogeneous media, it has been applied to model BHJ cells made of poly[2-methoxy-5-(3′,7′-dimethyloctyloxy)-*p*-phenylene vinylene] (OC_1C_{10}-PPV) blended with $PC_{60}BM$ [166]. For nonzero k_{f}, the field-dependence of k_{d} causes P to vary with the internal electric field and therefore with the external bias. If non-geminate recombination is weak, this field-dependence determines the course of the photocurrent as a function of applied voltage. Based on this assumption, Mihailetchi et al. concluded that in OC_1C_{10}-PPV:$PC_{60}BM$ only 60% of the bound CT states dissociate into free carriers at short-circuit conditions and room temperature. Field-assisted generation in PPV-based blends was recently confirmed by Mingebach et al. [167]. The Braun–Onsager model was also applied to describe the *J*/*V* characteristics of P3HT:PCBM solar cells [73, 168], but this analysis yielded long CT lifetimes of at least 100 ns [159].

The application of the model to P3HT:PCBM blends was challenged by the observation of efficient ultrafast free carrier generation in as-prepared and annealed P3HT:$PC_{60}BM$ thin films using transient absorption spectroscopy (TAS) with a subpicosecond time resolution [100, 169, 170]. Quenching of the excitons in the P3HT phase, accompanied by the appearance of a photoinduced absorption signal assigned to polarons, was shown to occur within 100 fs for as-prepared blends and within a few picoseconds in annealed blends. The slower build-up of the polaron population in the annealed sample was attributed to the dynamics of exciton diffusion to the BHJ. Figure 16 shows exemplary TAS traces for as-prepared and annealed P3HT:PCBM blends as a function of illumination fluence. Detailed analysis of the TAS experiments as a function of the pulse fluence suggested that exciton dissociation leads to two populations, free charges and bound polaron pairs, with the latter recombining geminately within only 2 ns [169]. These experiments ruled out the possibility that photogeneration in P3HT:PCBM blends involves a long-lived CT state and suggested that free carrier formation may not necessarily be assisted by the electric field. Interestingly, the thermal treatment of these chlorobenzene-cast blends had a rather small effect on the fraction of generated free carriers, which was 68 and 85% for the as-prepared and thermally annealed layers, respectively. Thus, despite a large difference in the PV performance, exciton-to-polaron conversion proceeds with comparable efficiency in both of these samples. In contrast, regiorandom P3HT blended with PCBM yielded a much smaller free carrier formation efficiency of only about 20%, while most

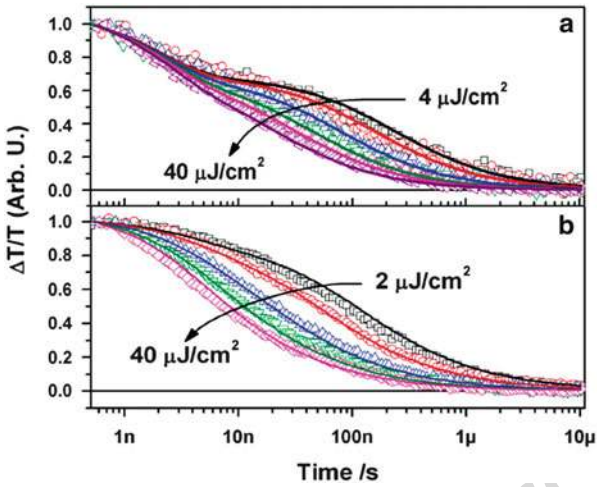

Fig. 16 Charge induced absorption decay (750–850 nm) for (**a**) as-prepared and (**b**) annealed 1:1 blends of regioregular P3HT and PCBM coated from chlorobenzene. The transients of the as-prepared device show a fluence-independent decay attributed to geminate recombination of strongly bound CT states at early times. The dynamics of both blends at longer times is entirely determined by the recombination of free polarons. *Lines* show global fits to a non-geminate recombination model including a density-dependent recombination coefficient. The data show conclusively that free carrier formation is rapid and that geminate recombination is completed within few nanoseconds. Reprinted (adapted) with permission from [169]. Copyright 2010 American Chemical Society

excitons formed strongly bound CT states that decayed geminately to the ground state within 2 ns.

Field-independent photogeneration in solvent-annealed P3HT:PCBM was unambiguously proven by Kniepert et al. using time-delayed collection field (TDCF) experiments [171]. In a TDCF measurement, as schematically shown in Fig. 17a, the sample is illuminated by a short laser pulse while being kept at a constant pre-bias voltage V_{pre}. After the delay time, t_d, a rectangular pulse with voltage V_{coll} is applied to sweep out all remaining free carriers. Therefore, TDCF is analogous to TAS with an electrical probe instead of an optical probe. In contrast to steady-state current–voltage measurements, classical time-of-flight experiments, or the photo-CELIV (charge extraction by a linearly increasing voltage upon photogeneration) technique, TDCF allows application of different biases during generation and collection of the charge carriers. To measure the field dependence of free carrier formation, TDCF experiments are performed with variable pre-bias, a short delay time, and a large collection field. Thereby, the delay time must be carefully chosen to ensure that geminate recombination is completed within the delay time. Also, the pulse fluence must be kept low to avoid non-geminate recombination prior to application of the collection bias. Provided that these conditions are safely met, the total collected charge as a function of the pre-bias

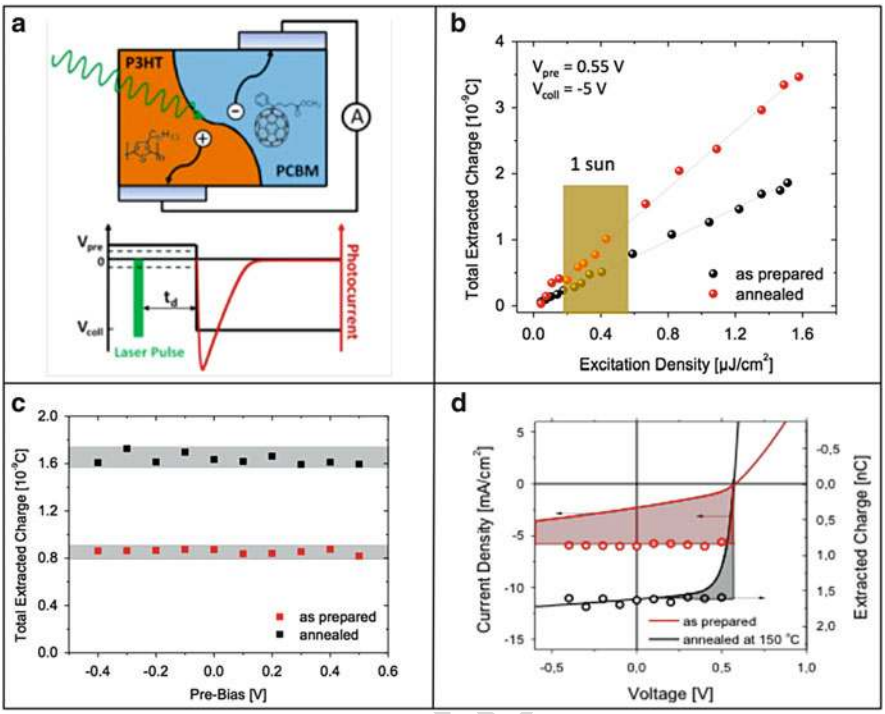

Fig. 17 (**a**) The TDCF experiment. A pre-bias V_{pre} is applied during illumination with a nanosecond laser pulse. After a given delay, rapid charge extraction is ensured by applying a large reverse bias V_{coll} [171]. (**b**) Total extracted charge Q_{tot} as a function of pulse fluence for as-prepared and annealed P3HT:PCBM. The time delay was 20 ns and the collection field was −5 V. Q_{tot} is perfectly linear in the fluence for both samples over the entire intensity range, ruling out losses due to non-geminate recombination. (**c**) Q_{tot} as a function of pre-bias for a pulse fluence of 0.7 μJ/cm^2. The generated charge is found to be independent of bias within an error of 10% (*grey areas*). (**d**) Comparison of the bias-dependent extracted charge and the steady-state *J*/*V* characteristics of the as-cast and annealed blend. In contrast to $Q_{tot}(V)$, the shape of the *J*/*V* characteristics of the two devices differs greatly, with the as-prepared device exhibiting a much lower fill factor. Therefore, incomplete charge extraction rather than field-dependent charge generation must be the main cause for the much poorer performance of the as-prepared device [172]

measures the field-dependence of free charge generation in competition with geminate recombination.

Field-independent free charge generation was also seen for P3HT:PCBM blends coated from chloroform, which had either been dried at room temperature (as-prepared) or annealed at 150°C for 15 min directly after spin-coating. These measurements were performed with a delay time of 20 ns, which is well above the lifetime of the CT state (as determined from TAS experiments, as described above). For such a short delay, the total collected charge Q_{tot} is perfectly linear over a wide range of pulse fluences, meaning that non-geminate recombination losses are

insignificant for the chosen parameters (Fig. 17b). The dependence of Q_{tot} versus V_{pre} measured for a moderate pulse fluence of 0.7 μJ/cm^2 is shown in Fig. 17c. The extracted free charge is independent of pre-bias (within 10%, see grey area in Fig. 17c) for both as-cast and thermally annealed blends, implying field-independent charge carrier generation. A very weak dependence of free carrier generation on the electric field was also seen in TDCF experiments performed on chlorobenzene-cast P3HT:PCBM, with and without thermal annealing [167, 173]. Further evidence for field-independent free carrier formation in thermally annealed P3HT:PCBM came from transient photoconductivity experiments [174, 175].

To summarize, field-independent generation is shown to be common to blends of regioregular P3HT with PCBM. The importance of this finding becomes evident when considering that the studied devices were processed under a variety of conditions (different solvents, thermal annealing, solvent annealing, different layer thicknesses), which resulted in different morphologies and, consequently, in a wide range of PV performance parameters.

Before discussing possible morphological pictures to explain these findings, we turn to the involvement of CT states in the exciton-to-polaron conversion in P3HT:PCBM blends. The observed insensitivity of free carrier generation to the internal electric field suggests that this process does not involve split-up of bound CT states. It has been proposed that the dissociation of P3HT excitons at the heterojunction generates "hot" CT states (Fig. 18a), which possess a sufficient amount of energy to overcome the Coulomb barrier without the aid of an electric field [169]. Interestingly, "colder" CT states in P3HT:PCBM can be directly excited by using photon energies of between 1.2 and 1.6 eV, which is below the energy of the vibronically relaxed S_1 exciton of P3HT. Lee and coworkers measured the external quantum efficiency and the absorption of annealed P3HT:PCBM over a wide range of photon energies [163]. The main result of these experiments is displayed in Fig. 18b. The EQE spectrum was fully reproduced by considering only the wavelength-dependent absorption of the organic layer in the device while keeping the internal quantum efficiency constant at around 80%. It was concluded that efficient free charge generation in P3HT:PCBM does not require the split-up of hot CT states, which is in contrast to the hot CT model outlined above. In accordance with the interpretation by Lee and coworkers, it was reported that the incident photon energy has no effect on the charge generation and recombination in either as-prepared or thermally annealed P3HT:PCBM blends [162]. These authors also showed that the shape of the EQE does not change with bias. Because free carrier generation is known to be independent of bias upon excitonic excitation, the dissociation of CT states must also be unaffected by the internal electric field.

An important observation by Lee et al. is that free charge generation is efficient, even when directly exciting the sub-bandgap CT state. Therefore, a driving force must exist that counterbalances the mutual Coulomb attraction of these geminate polaron pairs. One possible cause of this force is the energy landscape in these blends, arising from its particular three-phase morphology. As pointed out above, these blends consist of three phases: intermixed regions of P3HT and PCBM, domains of crystallized P3HT chains, and almost pure agglomerates of PCBM

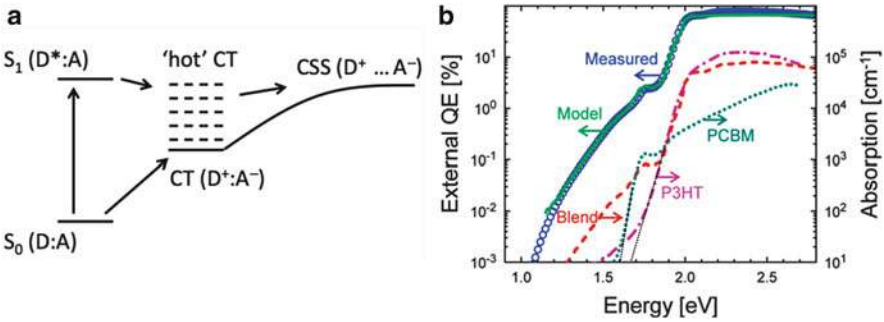

Fig. 18 (**a**) Generation of free charges either via a "hot" charge transfer (CT) state formed by S_1 exciton split-up or via a "cooler" CT state that is generated by direct excitation. Reprinted with permission from [162]. Copyright © 2012 Wiley-VCH Verlag GmbH & Co. KGaA, Weinheim. (**b**) Experimental EQE spectrum under short-circuit conditions (*circles*) compared with the absorption coefficient of solid P3HT, PCBM, and the 1:1 P3HT:PCBM blend. Also shown is the modeled EQE spectrum that assumed a constant IQE of 80% but a wavelength-dependent absorption (A) of the blend layer according to $A = A_0(1 - \exp(-2\alpha d))$, with α being the absorption coefficient and d the active layer thickness. Reprinted (adapted) with permission from [163]. Copyright 2010 American Chemical Society

molecules. P3HT chains within the mixed domains are believed to exhibit a twisted conformation, similar to chains in solution or in a solid sample of regiorandom P3HT. As these twisted chains exhibit lower HOMO energies than those in crystallites of planar P3HT [176], an energy gradient is established that drives holes out of the intermixed regions [177]. Similarly, Jamieson et al. pointed out recently that the larger electron affinity of PCBM molecules in pure fullerene aggregates compared to the intermixed domain assists free charge generation [178]. Polaron pairs generated in the intermixed regions are therefore prone to rapid dissociation into spatially separated charges, with the hole and electron residing on domains of the pure donor and acceptor, respectively (Fig. 19a). This model of a morphology-related driving force is consistent with the observation of efficient dissociation of even relaxed CT states, and it also provides a reasonable explanation for the inefficient non-geminate recombination of electrons and holes in annealed P3HT:PCBM blends.

The situation is different when considering excitons that are formed within ordered P3HT domains. Troisi and coworkers pointed out that because of the lower band gap of chain segments within the crystallites, these excitons are repelled by the more disordered donor–acceptor interface [179]. The authors therefore proposed that these excitons split via tunneling of the electron through layers of more distorted polymer chains at the interface into higher and partially delocalized states on the PCBM aggregates (see Fig. 19b). This long-range exciton dissociation results in a spatially separated electron–hole pair, stabilized by a more disordered interfacial region. In a subsequent publication, Caruso and Troisi considered the

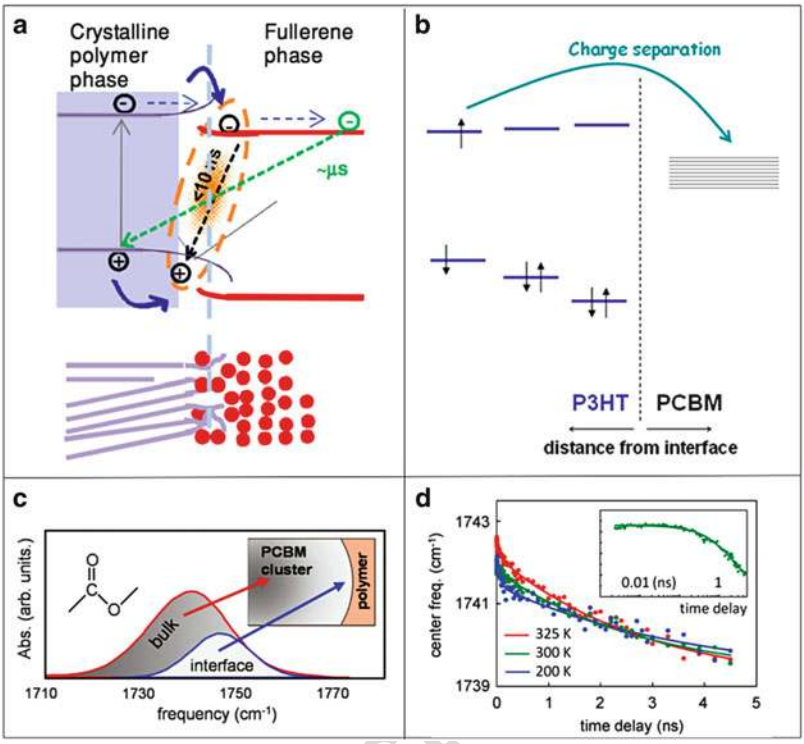

Fig. 19 (**a**) Split-up of geminate electron–hole pairs formed in the intermixed region between polymer-rich and fullerene-rich domains. Backbone twisting and disruption of intermolecular interactions raise the energies of electrons and holes in the intermixed region. Therefore, a morphological driving force is established that counterbalances the mutual Coulombic interaction of the geminate pair. Reprinted (adapted) with permission from [177]. Copyright © 2013 Wiley-VCH Verlag GmbH & Co. KGaA, Weinheim. (**b**) An exciton formed within the P3HT crystallite is repelled from the interface because chains at the boundary to PCBM exhibit a higher band gap. Exciton split-up can, however, occur via electron tunneling into partially delocalized states in the PCBM aggregates. Reprinted (adapted) with permission from [179]. Copyright 2011 American Chemical Society. (**c**) The frequency of the carbonyl stretch vibration of the PCBM is higher at the interfaces with conjugated polymers than of PCBM molecules in the interior of fullerene aggregates. Therefore, the dynamics of charge transfer spit-up in polymer:fullerene blends can be followed through the time dependence of the carbonyl vibration frequency after excitation in a transient visible/infrared experiment. Reprinted (adapted) with permission from [180]. Copyright 2010 American Chemical Society. (**d**) Time-dependence of the center frequency of the PCBM carbonyl stretch recorded at three different temperatures after pulsed excitation of a P3HT:PCBM blend film with 550 nm light. The independence of the transient on temperature is interpreted in terms of an activationless split-up of interfacial electron–hole pairs. Reprinted (adapted) with permission from [181]. Copyright 2012 American Chemical Society AU10

kinetics and energetics of the proposed process in greater detail [182]. For long-range transfer, the electron transfer rate k_{ET} scales approximately like $k_{ET}(R) = k_0 \exp(-\beta R)$ with distance R, where β is an attenuation factor. It is shown that tunneling through conjugated chains results in values of β as small as 0.2 $Å^{-1}$. 945 946 947 948

Under these conditions, k_{ET} for an exciton formed 23 Å from the interface (corresponding to six chains in the π-stacking direction) is on the order of 10^{12} s^{-1}, which leads to polaron formation on a time scale comparable with that found experimentally in annealed P3HT:PCBM.

In P3HT:PCBM, both mechanisms described above may contribute to free charge photogeneration. Tunneling, as proposed by Troisi and coworkers, is important when exciting the blend at 500–650 nm, where aggregated P3HT absorbs. On the other hand, sub-bandgap absorption excites CT states predominately in the intermixed region, and the split-up of these coulombically interacting electron–hole pairs benefits from the morphology-related driving force. One might, therefore, expect the IQE to depend on the excitation energy, which is apparently not the case in P3HT:PCBM. In a very recent work, Vandewal et al. demonstrated the IQE to be insensitive to excitation energy for various organic donor–acceptor BHJ systems [183]. It is proposed that photogeneration proceeds via the split-up of thermalized (electronically and vibronically relaxed) CT states at all illumination conditions, even if illumination primarily excites the donor or acceptor component. This situation was encountered in an inefficient blend with a pronounced field dependence of generation, but also for a highly efficient blend with field-independent generation. Accordingly, we propose that photogeneration in P3HT:PCBM is entirely governed by the efficient split-up of low-energy CT states.

We note that activationless free charge generation in P3HT:PCBM was unambiguously proven with ultrafast vibrational spectroscopy [180, 181]. It had previously been shown that the frequency of the carbonyl group in PCBM depends on the local environment: the vibration frequency of a PCBM molecule located in the interior of a fullerene cluster is lower than that of a PCBM molecule at the interface to the donor polymer [184] (see Fig. 19c). Therefore, the motion of the electron away from the heterojunction during charge separation can be monitored through a decrease in the carbonyl frequency. For P3HT mixed with PCBM, the time-dependence of the carbonyl center frequency was independent of the temperature, meaning that free charge formation via CT split-up does not require thermal activation (Fig. 19d) [181]. In agreement with this, TAS experiments presented by Mauer et al. showed free carrier generation in annealed regioregular (rr)-P3HT:PCBM blends to be independent of temperature [185], indicating again activationless geminate pair separation.

In conclusion, free charge generation in blends of regioregular P3HT with PCBM is independent of electric field and possibly temperature for a wide range of preparation conditions and efficiencies. Carrier formation seems to be equally efficient when CT states are formed via the split-up of singlet excitons at the BHJ or when they are generated directly via sub-bandgap excitation. The findings are explained by the complex morphology of these layers, which comprise pure and intermixed regions. The answer to the question of why the exciton-to-polaron conversion in rr-P3HT:PCBM blends is rather insensitive to the preparation conditions might lie in the fact that even samples as-cast from chloroform with very

poor performance exhibit a considerable concentration of P3HT aggregates, which guarantee efficient CT split-up at the local scale.

4.2 Charge Extraction Versus Non-geminate Recombination

As pointed out in the previous section, free carrier generation in P3HT:PCBM blends proceeds at the picosecond time scale, unassisted by the applied electric field. It must, therefore, be the free carrier recombination (non-geminate recombination) in competition with charge extraction that accounts for most of the photocurrent loss within the working regime of P3HT:PCBM blends.

The influence of non-geminate recombination on the J/V characteristics can be best understood by considering the current flowing through the device under steady-state illumination, $J_{\text{light}}(V)$, in terms of current densities of generation and of non-geminate loss:

$$J_{\text{light}}(V) = J_{\text{gen}}(V) - J_{\text{NG}}(V), \tag{7}$$

where J_{gen} is the generation current density (the generated free charge per unit area and time) and J_{NG} the loss current density including non-geminate recombination in the bulk and carrier extraction at the wrong contact (electrons leaving the device via the anode or holes via the cathode). J_{NG} can be written as [186]:

$$J_{\text{NG}}(V) = ed\frac{n}{\tau(n)}, \tag{8}$$

with $\tau(n)$ being the inverse recombination rate parametric in the carrier density n as given by:

$$\frac{1}{\tau(n)} = \gamma n. \tag{9}$$

Here, γ is the non-geminate recombination coefficient and $\lambda+1$ the order of recombination. Clearly, non-geminate losses become more significant at higher carrier density n, e.g., at low fields or as a result of low mobilities, and for a high γ. In the ideal case, free carriers recombine either with trapped charges (Schottky–Reed–Hall recombination; SRH) or with free carriers of the opposite sign (bimolecular recombination). In the first case, $\lambda+1=1$ and the lifetime of the free carrier does not depend on carrier density. In contrast, for bimolecular recombination, $\lambda+1=2$ and an increased density of photogenerated charge accelerates recombination. Although there is some evidence that the SRH process cannot be neglected in P3HT:PCBM devices [175, 187], the consensus is now that the non-geminate photocurrent loss is mainly due to bimolecular recombination.

Various methods have been applied to P3HT:PCBM in order to quantify the parameters that describe non-geminate recombination (see, e.g., [187–194]). Knowledge about γ and $\lambda+1$ was mostly derived from transient pump-probe measurements (see, e.g., [169, 189, 195]). In these experiments, a short laser pulse excites the sample and the fate of the photogenerated charge is followed by measuring the transient polaron-induced absorption signal. In a homogenous medium with low carrier mobility, the decrease in carrier density via non-geminate recombination is predicted to follow Langevin-type bimolecular recombination:

$$\frac{\mathrm{d}n}{\mathrm{d}t} = -\frac{n}{\tau(n)} = -\gamma_{\mathrm{L}} n^2 \tag{10}$$

with $\lambda+1=2$ and the Langevin recombination coefficient $\gamma_{\mathrm{L}} = e(\mu_{\mathrm{e}}+\mu_{\mathrm{h}})/\varepsilon_0\varepsilon_{\mathrm{r}}$. However, most publications show that the free carrier dynamics in bulk heterojunction devices is not guided by simple Langevin-type recombination. TAS transients of annealed P3HT:PCBM could be described only when assuming a higher order recombination process with $\frac{dn}{dt} \propto -n^3$. This finding was explained by bimolecular recombination $\frac{dn}{dt} \propto -\gamma(n)n^2$ with a recombination coefficient that itself depends on charge density [189]. Earlier work by Nelson suggested that charge recombination in polymer:fullerene blends occurs via diffusive motion of polarons in the presence of an exponential density of traps [196]. Increasing the density of photogenerated charge fills these traps and thus accelerates non-geminate recombination. Carrier-dependent mobilities in P3HT:PCBM blends were independently proven by two groups [197, 198]. TAS experiments performed by Shuttle et al. also showed that bimolecular recombination in annealed P3HT:PCBM blends is severely slowed down compared with the Langevin limit, with values of $\gamma/\gamma_{\mathrm{L}}$ of the order of 10^{-2}–10^{-3}. This finding is in agreement with earlier work by Pivrikas et al. [188]. Suppressed recombination was attributed to the particular nanomorphology of these blends that consists of an interpenetrating network of spatially separated (and energetically separated) pathways for electrons and holes. The basic finding of a higher order but suppressed recombination, compared with the Langevin limit, was consistently seen in follow-up TAS experiments on both as-prepared and annealed P3HT:PCBM blends [169, 185, 195, 199], and was confirmed by flash photolysis and time resolved microwave conductivity experiments [191].

One disadvantage of these all-optical pump-probe techniques is that they require high excitation densities and thus do not provide information on the fraction of charge surviving recombination under different bias conditions. An elegant approach to quantify these processes is to perform TDCF measurements with increasing delay time. Integration of the transients during delay and during collection yields the quantities $Q_{\mathrm{pre}}(t_{\mathrm{d}})$ and $Q_{\mathrm{coll}}(t_{\mathrm{d}})$, respectively, from which the total collected charge can be calculated via $Q_{\mathrm{tot}}(t_{\mathrm{d}}) = Q_{\mathrm{pre}}(t_{\mathrm{d}}) + Q_{\mathrm{coll}}(t_{\mathrm{d}})$. The exemple shown in Fig. 20 is the dependence of these quantities as a function of delay time for

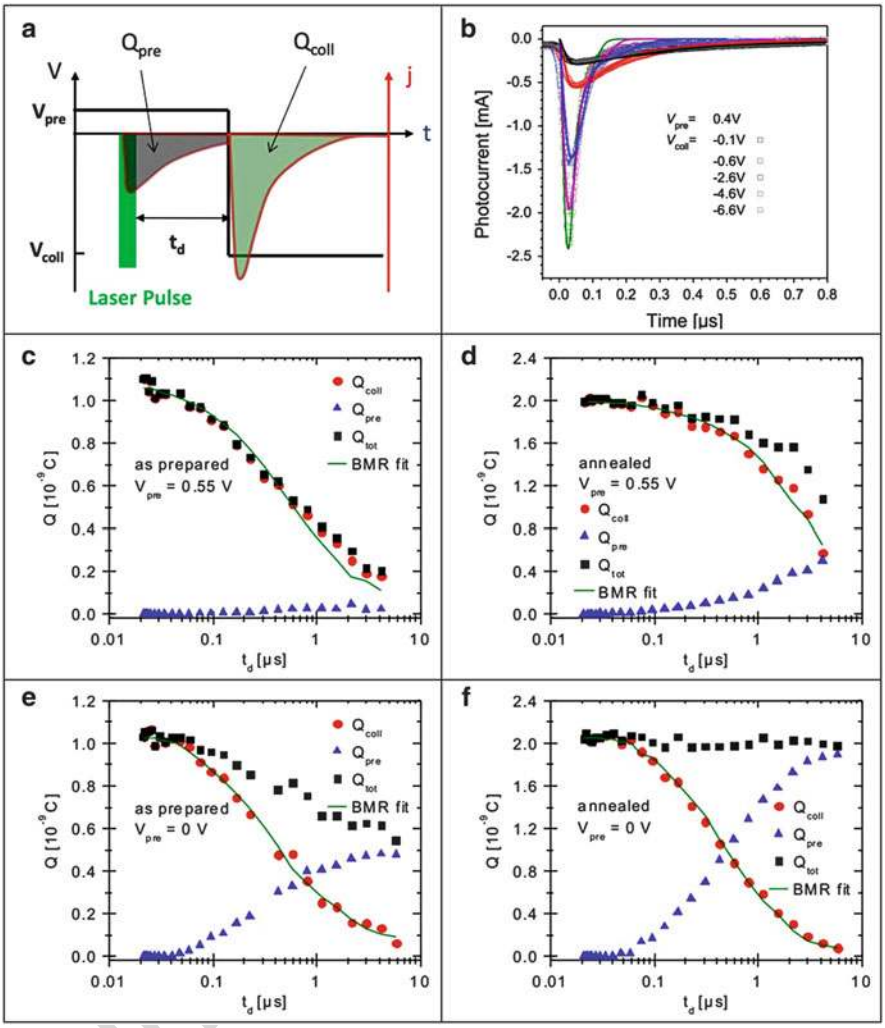

Fig. 20 Determination of the coefficient of bimolecular recombination by performing TDCF experiments with variable delay between the excitation pulse and application of the collection bias. (**a**) Scheme of the experiment. (**b**) Experimental TDCF photocurrent transients (*open squares*) measured on a 200 nm thick layer of slow-dried P3HT:PCBM (1:1) during application of different collection biases V_{coll}. The collection bias was applied 150 ns after the laser pulse ($t = 0$ in this graph). *Solid lines* show fits to the data using a numerical drift diffusion model with constant electron and hole mobilities. A noteworthy observation is that charges can be fully extracted from these layers within a few hundreds of nanoseconds for a sufficiently high collection bias [171]. (**c–f**) Q_{pre}, Q_{coll}, and Q_{tot} plotted as a function of the delay time t_d for as-prepared and thermally annealed chloroform-cast P3HT:PCBM, and with the pre-bias V_{pre} set either to 0.55 V (near open circuit) or to 0 V (short-circuit conditions) [172]. *Solid lines* show fits with an iterative model that considers bimolecular recombination of free charges in competition with their extraction

chloroform as-cast and annealed P3HT:PCBM for a pre-bias of 0.55 and 0 V. In all cases, the increase in Q_{pre} with t_d is due to field-induced extraction of photogenerated carriers, leaving less charge available when the collection bias is switched on. Decreasing the pre-bias, and thereby increasing the internal field, accelerates the sweep-out of carriers, reducing the amount of available charge upon starting collection after the delay time t_d. If V_{coll} is chosen to be sufficiently high to avoid recombination during collection, the course of Q_{tot} (t_d) is a measure of the total non-geminate recombination loss during delay.

This set of data displays some important differences between the as-prepared and annealed samples. First, the extraction of charges from the annealed layers is faster and far more efficient. For example, half of the initially photogenerated carriers are swept out of the device at 0 V within 1 ms and non-geminate recombination is almost absent at short-circuit conditions (Q_{tot} is essentially independent of t_d). When raising the bias close to $V_{oc,}$ extraction is slowed down and the carrier density in the sample declines as a result of non-geminate recombination. For the as-prepared layer, non-geminate recombination is seen for both short-circuit and open-circuit conditions, rendering extraction inefficient for both bias conditions. Also, extraction is considerably slower and recombination is more efficient in these samples.

Because Q_{coll} is a direct measure of the charge present in the layer at a delay time t_d, the recombination dynamics can be determined via an iterative procedure [171]. For the data shown in Fig. 20, this analysis yields $\gamma = 3.5 \times 10^{-17}$ m^3 s^{-1} and $\gamma = 1.2 \times 10^{-18}$ m^3 s^{-1} for the chloroform as-cast and the annealed P3HT:PCBM layer, respectively. The value for the annealed sample agrees very well with the bimolecular recombination coefficient measured by TAS at carrier densities typical for steady-state AM1.5 illumination (see, e.g., [189, 195]). To compare these values to the Langevin limit, the mobilities of the electrons and the holes in the blend must be known. Information on these quantities can be gained from drift-diffusion simulations of the photocurrent transients with different collection biases (see Fig. 20b). This yields mobilities of 1.2×10^{-7} m^2 V^{-1} s^{-1} and 1.7×10^{-7} m^2 V^{-1} s^{-1} for the faster carrier in the as-prepared and annealed blend. Assuming that the faster carrier determines non-geminate recombination dynamics, recombination is reduced by three orders of magnitude compared with the Langevin limit in the annealed layer whereas it is still suppressed by a factor of 20 in the as-cast blend.

Although suppressed bimolecular recombination in P3HT:PCBM blends has been seen in numerous experimental studies, there is still no consistent model to explain values of the Langevin reduction factor γ/γ_L as low as 10^{-4}. Koster et al. pointed out that if electrons and holes move in separate regions and recombination takes place only at the donor–acceptor interface, non-geminate recombination kinetics will be determined not by the faster but by the slower carrier: $\gamma = \frac{e}{\varepsilon}\min(\mu_e, \mu_h)$ [200]. The analysis of space-charge-limited currents (SCLC) in chloroform-cast P3HT:PCBM blends revealed holes to be less mobile than electrons, particularly for low annealing temperatures [73, 171]. This view has been

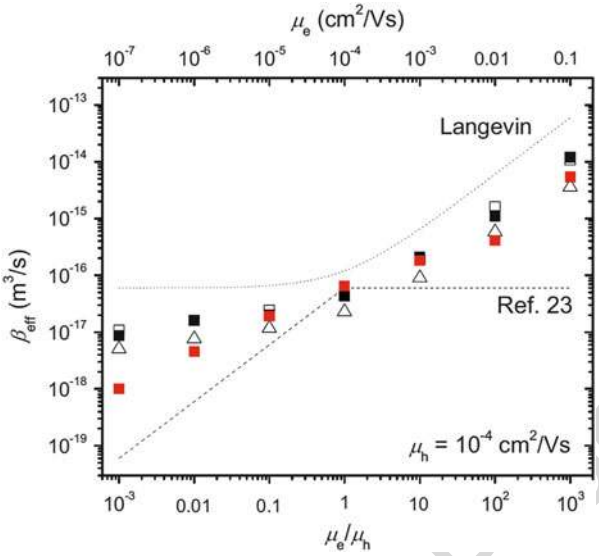

Fig. 21 Effective bimolecular recombination coefficient β_{eff} calculated by Monte Carlo modeling of a phase-separated blend with an average feature size of 4 (*black*) and 35 nm (*red*). Simulations were performed in the absence of energetic disorder (*squares*) or by assuming a Gaussian-type DOS with a width $\sigma = 75$ meV (*triangles*). *Open symbols* represent an electric field $F = 0$ and *closed symbols* are for $F = 10^7$ V/m. The Langevin limit is shown by the *dotted line* and the *dashed line* is for Langevin-type recombination limited by the slower carrier. *Ref 23* refers to the model in Shuttle et al. [202]. In all cases, the hole mobility was 10^{-4} cm^2/V s. Reprinted with permission from [201]. Copyright 2008 by the American Physical Society

challenged by Monte Carlo simulations of non-geminate recombination in phase-separated blends [201]. Although these calculations allowed carriers to recombine only at the interface, the non-geminate recombination coefficient was less affected by the slower carrier mobility than Koster and coworkers had proposed (see Fig. 21). The surprisingly weak effect of the slow carrier mobility on the recombination coefficient was attributed to the fact that carriers are distributed homogeneously in their respective phases, meaning that there is a population of the slower carriers close enough to the interface to be able to recombine with the faster carriers. It is, therefore, most likely that the reduced recombination originates mainly from the energetic barrier formed at the heterojunction due to increased morphological disorder in the interfacial region; however, other reasons such as an inhomogeneous distribution of electrons and holes in the device or unbalanced transport might also account for this effect [203, 204].

The strongly suppressed non-geminate recombination is highly beneficial for device performance as it prevents free charges from recombining prior to extraction to the electrodes. Quantitative information on the photocurrent loss due to non-geminate recombination, J_{NG}, can be obtained by combining transient photovoltage (TPV) with charge extraction (CE) measurements, as shown by

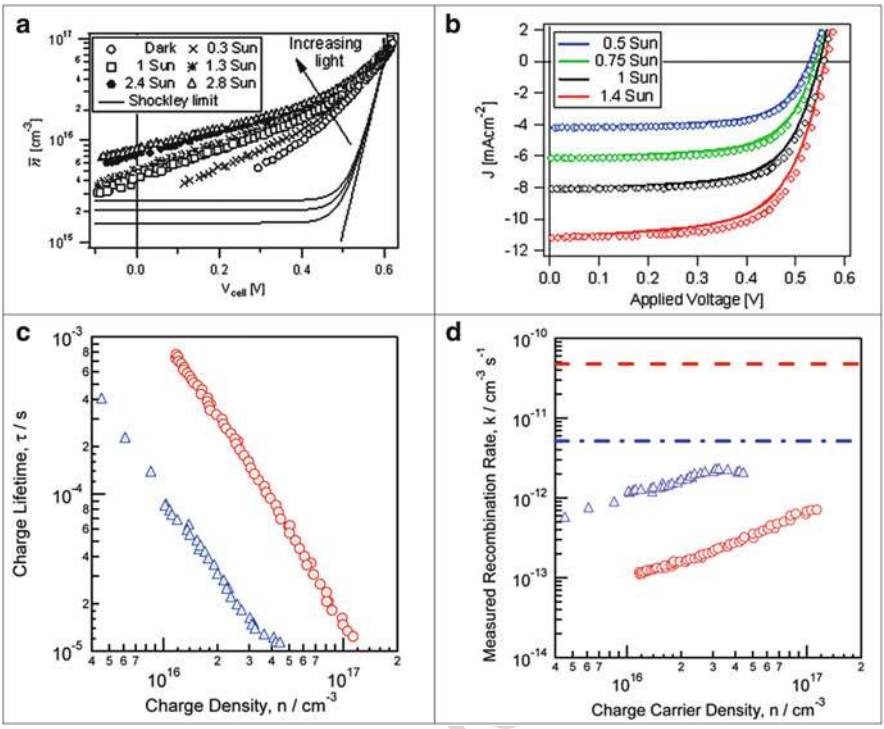

Fig. 22 (**a**) Average charge density in an annealed P3HT:PCBM layer (coated from xylene solution) as a function of cell voltage and illumination intensity as measured by charge extraction (CE). (**b**) Reconstruction of the measured current–voltage characteristics under steady-state illumination from Eqs. (7) and (8), with the carrier densities shown in (**a**) and carrier density-dependent recombination rates measured with TPV. (**c**) Charge carrier lifetimes and (**d**) bimolecular recombination coefficients as a function of carrier density as obtained by CE and TPV measurements on pristine (*blue triangles*) and thermally annealed (*red circles*) P3HT:PCBM blends. (**a**, **b**) reprinted (adapted) with permission from [207]. (**c**, **d**) reprinted (adapted) with permission from [205]. Copyright 2010 American Chemical Society

Shuttle and coworkers [205]. In TPV, the layer is under steady-state illumination with white light of appropriate intensity and the voltage across the device is measured with a large serial resistor. Therefore, the sample is under quasi-open-circuit conditions. The sample is then illuminated with a short and weak laser pulse, which increases the charge carrier density and thus causes the voltage across the device to increase. The decay of the transient photovoltage back to its steady-state value is, therefore, a direct measure of the non-geminate recombination rate [189]. To determine the charge within the illuminated blend layer by CE, the device is held under steady-state illumination at a certain bias and then is switched to short circuit (zero bias) while at the same time the light is switched off. The current transient after the switch to short-circuit conditions is integrated and corrected for the capacitive charge [206].

As shown in Fig. 22, the carrier density within the blend layer changes with illumination intensity I, cell voltage V, and temperature T. Combining $n(I, V, T)$ with charge carrier lifetime data determined with TPV at comparable carrier densities allows calculation of the loss current density J_{NG} via Eq. (8). Finally, the current characteristics under steady-state illumination are reconstructed with the assumption of a field-independent generation current density, $J_{gen} \cong J_{sc}$. This approach has been successfully applied to both as-prepared and annealed P3HT:PCBM layers [173, 205]. The data in Fig. 22c, d also show that the annealed device displays larger carrier lifetimes and lower recombination coefficients than the as-cast sample at comparable carrier densities. This has been quoted as the main cause for the superior performance of the thermally treated sample [173, 205].

We will, finally, comment briefly on the importance of establishing high electron and hole mobilities in P3HT:PCBM blends. Clearly, a high mobility of both types of carriers ensures rapid extraction of photogenerated charge out of the blend layers, rendering these carriers less vulnerable to recombination loss. Goodman and Rose [208] and later Mihailetchi et al. [209] stated that unequal carrier mobilities cause formation of space charge within the active layer, which renders part of the blend essentially field-free. As a consequence, the extracted current becomes significantly smaller than the photogenerated current:

$$J_{ph} = q\left(\frac{9\varepsilon_0\varepsilon_r\mu_{min}}{8q}\right)^{1/4} G^{0.75}V^{0.5}. \quad (11)$$

Here, G is the generation rate and μ_{min} the mobility of the slower carrier. A characteristic feature of space-charge-limited photocurrents is that they possesses a sublinear dependence on generation rate (illumination intensity). As demonstrated in Fig. 23, as-cast blends of chloroform-coated P3HT:PCBM blends exhibit reasonable electron mobilities but very poor hole mobilities. As pointed out in Sect. 3, the poor hole transport in these as-prepared devices is a result of the low degree of crystallinity in combination with poor ordering within the polymer aggregates. As a consequence, the performance of this device is space-charge limited, as evidenced by the sublinear increase in photocurrent with light intensity. Annealing the device improves μ_h, thereby reducing the mobility imbalance, which concurrently results in a large improvement in device performance. Poor hole mobility was also identified as the main cause of the poor performance of devices made from low molecular weight P3HT [57, 210].

To conclude this section, non-geminate recombination is identified as the main loss channel in poorly performing as-prepared P3HT:PCBM blends. This is for two reasons: First, the coefficient for bimolecular recombination is larger in as-prepared blends, possibly caused by a higher degree of intermixing of the donor and acceptor component. Second and more important, as-prepared P3HT:PCBM blends exhibit lower mobilities, rendering free charges more vulnerable to non-geminate recombination and causing severe space–charge effects at solar illumination conditions.

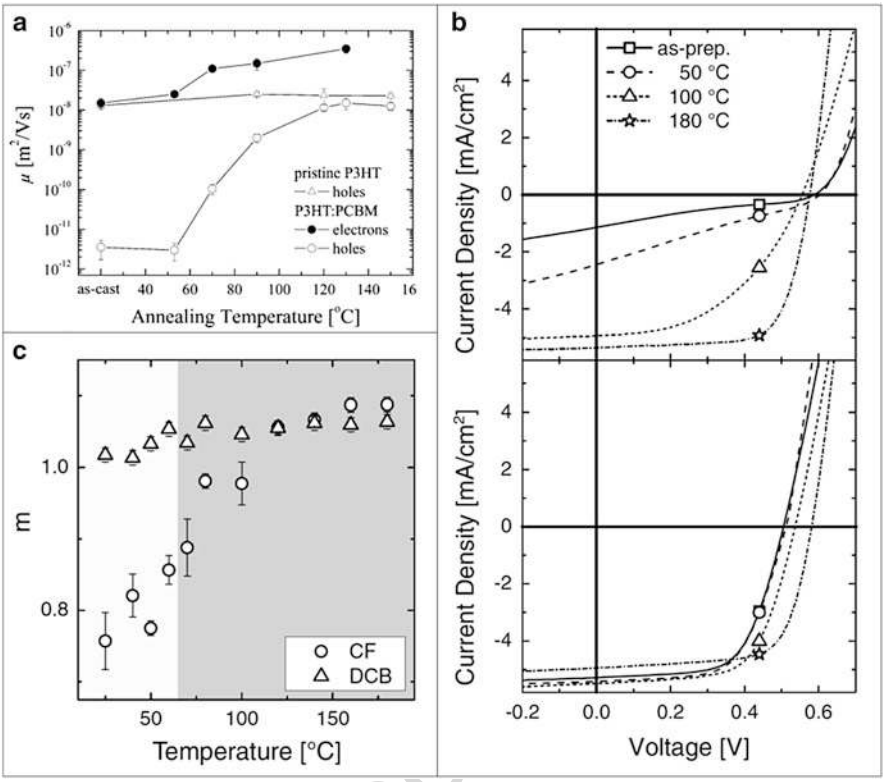

Fig. 23 (**a**) Zero-field mobilities for electrons (*closed circles*) and holes (*open circles*) at room temperature for chloroform-coated 1:1 P3HT:PCBM blends as a function of postproduction annealing temperature. Also shown is the hole mobility in pure P3HT (*triangles*). Mobilities were derived from space-charge-limited current measurements on the corresponding unipolar devices. Reprinted with permission from [73]. Copyright © 2006 Wiley-VCH Verlag GmbH & Co. KGaA, Weinheim. (**c**) Slope of the power-law increase *m* in the photocurrent as a function of illumination intensity in a log–log representation as a function of annealing temperature for a 100 nm thick P3HT:PCBM blend coated from chloroform (*CF*) or dichlorobenzene (*DCB*) [146]. (**b**) *J*/*V* characteristics under simulated AM1.5G illumination for the devices in (**c**) for selected annealing temperatures cast from chloroform (*top*) and dichlorobenzene (*bottom*) [146]

5 Summary, Conclusions, and Outlook

From 2003 to 2013, P3HT:PCBM was the "fruit fly" system to study for understanding organic photovoltaic properties. The understanding of these properties has not been straightforward because of the complex way that P3HT and PCBM interact with each other, with themselves, and with the substrates. In particular, mixed BHJ films, which self-assemble from solution in the length range from 10^{-10} to 10^{-5} m, have a hierarchical variety of film features. Because the film forms via self-assembly, changing the fabrication conditions that affect the solvation of

one component more than the other can lead to a dizzying variety of optical, electrical, and morphological features that are not particularly easy to measure and difficult to interpret. Further complicating the literature are polymer samples with a variety of molecular weights and regioregularities. Mixtures have different mixing ratios, and are cast from different solvents.

Regarding charge carrier dynamics, charge generation in P3HT:PCBM was shown to be ultrafast and activationless, even when exciting low energy CT states. Therefore, formation of free charge must be driven by particular energetics at the mesoscale, which counterbalance the Coulomb attraction of the geminate pair forming the CT state. Recent quantum dynamic simulations suggest that delocalization of electrons and holes on well-ordered domains assists free charge generation by reducing the Coulomb binding of interfacial CT states [211]. Because most blends of regioregular P3HT with PCBM studied so far exhibit a significant fraction of crystallized P3HT chains, charge delocalization might explain why free charge generation is field-independent, irrespective of the exact preparation scheme. A second particularity of well-performing P3HT:PCBM devices is highly reduced non-geminate recombination. In comparison to the Langevin limit of electron–hole recombination in an isotropic homogeneous medium, free charge recombination in P3HT:PCBM is slowed down by a factor of 100–1,000. This vast reduction in recombination speed allows the use of thick and well-absorbing blend layers, without risking inefficient charge extraction and low fill factors.

In total, it took thousands of people 10 years, and more than 10^3 published articles, to reach this level of understanding about how P3HT:PCBM BHJ OPV devices really function, how the materials self-assemble, and how to alter the self-assembly process via fabrication conditions to achieve a desired morphology for efficient charge generation and extraction. The lessons learned from P3HT:PCBM are being applied to a variety of new polymers and fullerenes with the goal of making better OPV devices. Mixed solvents, a high level of synthesis control, and highly specialized methods to measure the morphology are now necessary to produce new insights into BHJ function. Thus, the low hanging fruit have been eaten.

Also, advanced electronic and optical measurements are needed to describe common features of BHJ OPV devices. Clear (although complicated) optical and electrical models have been developed that do a good job of predicting the efficiency and other *I*/*V* characteristics of a given donor–acceptor mixture. AU12

So is OPV all figured out? If not, what is next? Now that the science of determining how to synthesize high efficiency materials, how to process the mixtures, how to fabricate the devices, how to characterize each step of the film formation, and how to measure the optical and electrical features of the device have been established, we still need to reliably engineer good devices. In particular, it is necessary to determine the following:

- How to coat BHJ layers quickly and without defects
- How to protect films against O_2 and UV light, which destroy device function

– What other impurities degrade BHJ function under the conditions of heat, light, electric field, and mechanical stress.
– What electrode materials are flexible, transparent, low resistance, and provide greater device longevity
– How to fabricate multiple BHJ layers in series (which is difficult due to the problem of dissolving previously deposited layers.)

The future of OPV research is bright and active, but the challenges that remain require continued increases in our understanding of the device complexity. Measurements will be even harder, because we will be searching for the low concentration impurity states (at 1 ppt to 1 ppm) that degrade device function, rather than assuming that these impurities either do not exist or are not important.

References

AU13
AU14

1. Allan RP, Soden BJ (2008) Science 321:1481–1484
2. Emanuel K (2005) Nature 436:686–688
3. Webster PJ, Holland GJ, Curry JA, Chang HR (2005) Science 309:1844–1846
4. Wentz FJ, Ricciardulli L, Hilburn K, Mears C (2007) Science 317:233–235
5. Shrotriya V, Li G, Yao Y, Moriarty T, Emery K, Yang Y (2006) Adv Funct Mater 16:2016–2023
6. Reese MO, Gevorgyan SA, Jorgensen M, Bundgaard E, Kurtz SR, Ginley DS, Olson DC, Lloyd MT, Moryillo P, Katz EA, Elschner A, Haillant O, Currier TR, Shrotriya V, Hermenau M, Riede M, Kirov KR, Trimmel G, Rath T, Inganas O, Zhang F, Andersson M, Tvingstedt K, Lira-Cantu M, Laird D, McGuiness C, Gowrisanker S, Pannone M, Xiao M, Hauch J, Steim R, DeLongchamp DM, Roesch R, Hoppe H, Espinosa N, Urbina A, Yaman-Uzunoglu G, Bonekamp J-B, van Breemen AJJM, Girotto C, Voroshazi E, Krebs FC (2011) Sol Energ Mat Sol C 95:1253–1267
7. Shockley W, Queisser HJ (1961) J Appl Phys 32:510–519
8. Peumans P, Yakimov A, Forrest SR (2003) J Appl Phys 93:3693–3723
9. Veldman D, Meskers SCJ, Janssen RAJ (2009) Adv Funct Mater 19:1939–1948
10. Scharber MC, Wuhlbacher D, Koppe M, Denk P, Waldauf C, Heeger AJ, Brabec CL (2006) Adv Mater 18:789–794
11. Koster LJA, Mihailetchi VD, Blom PWM (2006) Appl Phys Lett 88:093511
12. SolarServer.com (2012) Organic photovoltaics: Polyera reaches 9.1% efficiency with a polymer/fullerene cell. http://www.solarserver.com/solar-magazine/solar-news/archive-2012/2012/kw05/organic-photovoltaics-polyera-reaches-91-efficiency-with-a-polymerfullerene-cell.html (accessed 2 July 2014)
13. Krebs FC (2008) Polymer photovoltaics: a practical approach. SPIE, Bellingham
14. Krebs FC, Fyenbo J, Tanenbaum DM, Gevorgyan SA, Andriessen R, van Remoortere B, Galagan Y, Jorgensen M (2011) Energy Environ Sci 4:4116–4123
15. Krebs FC, Gevorgyan SA, Alstrup J (2009) J Mater Chem 19:5442–5451
16. Krebs FC (2009) Org Electron 10:761–768
17. Krebs FC (2009) Sol Energ Mat Sol C 93:394–412
18. Krebs FC (2009) Sol Energ Mat Sol C 93:465–475
19. Krebs FC, Jorgensen M, Norrman K, Hagemann O, Alstrup J, Nielsen TD, Fyenbo J, Larsen K, Kristensen J (2009) Sol Energ Mat Sol C 93:422–441
20. Shaheen SE, Radspinner R, Peyghambarian N, Jabbour GE (2001) Appl Phys Lett 79:2996–2998

21. Steirer KX, Reese MO, Rupert BL, Kopidakis N, Olson DC, Collins RT, Ginley DS (2009) Sol Energ Mat Sol C 93:447–453
22. Hoth CN, Steim R, Schilinsky P, Choulis SA, Tedde SF, Hayden O, Brabec CJ (2009) Org Electron 10:587–593
23. Hau SK, Yip H-L, Leong K, Jen AKY (2009) Org Electron 10:719–723
24. Girotto C, Rand BP, Genoe J, Heremans P (2009) Sol Energ Mat Sol C 93:454–458
25. Lim YF, Lee S, Herman DJ, Lloyd MT, Anthony JE, Malliaras GG (2008) Appl Phys Lett 93:193301
26. Green R, Morfa A, Ferguson AJ, Kopidakis N, Rumbles G, Shaheen SE (2008) Appl Phys Lett 92:033301
27. Vak D, Kim S-S, Jo J, Oh S-H, Na S-I, Kim J, Kim D-Y (2007) Appl Phys Lett 91:081102
28. Arias AC, MacKenzie JD, McCulloch I, Rivnay J, Salleo A (2010) Chem Rev 110:3–24
29. Mativetsky JM, Loo Y-L (2012) AIChE J 58:3280–3288
30. Moulé AJ (2010) Curr Opin Sol State Mat Sci 14:123–130
31. Tang CW (1986) Appl Phys Lett 48:183–185
32. Sariciftci NS, Smilowitz L, Heeger AJ, Wudl F (1992) Science 258:1474–1476
33. Halls JJM, Walsh CA, Greenham NC, Marseglia EA, Friend RH, Moratti SC, Holmes AB (1995) Nature 376:498–500
34. Yu G, Gao J, Hummelen JC, Wudl F, Heeger AJ (1995) Science 270:1789–1791
35. Padinger F, Rittberger RS, Sariciftci NS (2003) Adv Funct Mater 13:85–88
36. Shaheen SE, Brabec CJ, Sariciftci NS, Padinger F, Fromherz T, Hummelen JC (2001) Appl Phys Lett 78:841–843
37. Chen JW, Cao Y (2009) Acc Chem Res 42:1709–1718
38. Li G, Zhu R, Yang Y (2012) Nat Photon 6:153–161
39. Liang Y, Xu Z, Xia J, Tsai S-T, Wu Y, Li G, Ray C, Yu L (2010) Adv Mater 22:E135–E138
40. DeLongchamp DM, Kline RJ, Herzing A (2012) Energy Environ Sci 5:5980–5993
41. Chen W, Nikiforov MP, Darling SB (2012) Energy Environ Sci 5:8045–8074
42. Ma W, Yang C, Gong X, Lee K, Heeger AJ (2005) Adv Funct Mater 15:1617–1622
43. Li G, Shrotriya V, Huang J, Yao Y, Moriarty T, Emery K, Yang Y (2005) Nat Mater 4:864–868
44. Peet J, Kim JY, Coates NE, Ma WL, Moses D, Heeger AJ, Bazan GC (2007) Nat Mater 6:497–500
45. Moulé AJ, Meerholz K (2008) Adv Mater 20:240–245
46. Reyes-Reyes M, Kim K, Carroll DL (2005) Appl Phys Lett 87:083506
47. Ihn KJ, Moulton J, Smith P (1993) J Polym Sci B Polym Phys 31:735–742
48. Bouman MM, Havinga EE, Janssen RAJ, Meijer EW (1994) Mol Cryst Liquid Cryst Sci Technol A 256:439–448
49. Wu ZY, Petzold A, Henze T, Thurn-Albrecht T, Lohwasser RH, Sommer M, Thelakkat M (2010) Macromolecules 43:4646–4653
50. Koppe M, Brabec CJ, Heiml S, Schausberger A, Duffy W, Heeney M, McCulloch I (2009) Macromolecules 42:4661–4666
51. Brinkmann M, Rannou P (2009) Macromolecules 42:1125–1130
52. Ballantyne AM, Chen L, Dane J, Hammant T, Braun FM, Heeney M, Duffy W, McCulloch I, Bradley DDC, Nelson J (2008) Adv Funct Mater 18:2373–2380
53. Brinkmann M, Rannou P (2007) Adv Funct Mater 17:101–108
54. Zen A, Saphiannikova M, Neher D, Grenzer J, Grigorian S, Pietsch U, Asawapirom U, Janietz S, Scherf U, Lieberwirth I, Wegner G (2006) Macromolecules 39:2162–2171
55. Hiorns RC, de Bettignies R, Leroy J, Bailly S, Firon M, Sentein C, Preud'homme H, Dagron-Lartigau C (2006) Eur Phys J 36:295–300
56. Hiorns RC, De Bettignies R, Leroy J, Bailly S, Firon M, Sentein C, Khoukh A, Preud'homme H, Dagron-Lartigau C (2006) Adv Funct Mater 16:2263–2273
57. Schilinsky P, Asawapirom U, Scherf U, Biele M, Brabec CJ (2005) Chem Mater 17:2175–2180

58. Kline RJ, McGehee MD, Kadnikova EN, Liu JS, Frechet JMJ, Toney MF (2005) Macromolecules 38:3312–3319
59. Zen A, Pflaum J, Hirschmann S, Zhuang W, Jaiser F, Asawapirom U, Rabe JP, Scherf U, Neher D (2004) Adv Funct Mater 14:757–764
60. Kline RJ, McGehee MD, Kadnikova EN, Liu JS, Frechet JMJ (2003) Adv Mater 15:1519–1522
61. Trznadel M, Pron A, Zagorska M (1998) Macromolecules 31:5051–5058
62. Scharsich C, Lohwasser RH, Sommer M, Asawapirom U, Scherf U, Thelakkat M, Neher D, Koehler A (2012) J Polym Sci B Polym Phys 50:442–453
63. Roehling JD, Arslan I, Moulé AJ (2012) J Mater Chem 22:2498–2506
64. Berson S, De Bettignies R, Bailly S, Guillerez S (2007) Adv Funct Mater 17:1377–1384
65. Yin W, Dadmun M (2011) ACS Nano 5:4756–4768
66. Tremel K, Ludwigs S (2014) Morphology of P3HT in thin films in relation to optical and electrical properties. Adv Polym Sci doi: 10.1007/12_2014_288
67. Kim Y, Cook S, Tuladhar SM, Choulis SA, Nelson J, Durrant JR, Bradley DDC, Giles M, McCulloch I, Ha CS, Ree M (2006) Nat Mater 5:197–203
68. Hoth CN, Choulis SA, Schilinsky P, Brabec CJ (2009) J Mater Chem 19:5398–5404
69. Hoppe H, Sariciftci NS (2006) J Mater Chem 16:45–61
70. Moulé AJ, Bonekamp JB, Meerholz K (2006) J Appl Phys 100:094503
71. Clark J, Silva C, Friend RH, Spano FC (2007) Phys Rev Lett 98:206406
72. Niles ET, Roehling JD, Yamagata H, Wise AJ, Spano FC, Moulé AJ, Grey JK (2012) J Phys Chem Lett 3:259–263
73. Mihailetchi VD, Xie HX, de Boer B, Koster LJA, Blom PWM (2006) Adv Funct Mater 16:699–708
74. Blom PWM, Mihailetchi VD, Koster LJA, Markov DE (2007) Adv Mater 19:1551–1566
75. Drees M, Davis RM, Heflin JR (2004) Phys Rev B 69:165320
76. Li G, Shrotriya V, Yao Y, Yang Y (2005) J Appl Phys 98:043704
77. Lenes M, Koster LJA, Mihailetchi VD, Blom PWM (2006) Appl Phys Lett 88:243502
78. Hoppe H, Shokhovets S, Gobsch G (2007) Phys Status Solidi Rapid Res Lett 1:R40–R42
79. van Bavel S, Sourty E, de With G, Frolic K, Loos J (2009) Macromolecules 42:7396–7403
80. Jin H, Olkkonen J, Tuomikoski M, Kopola P, Maaninen A, Hast J (2010) Sol Energ Mat Sol C 94:465–470
81. Parmer JE, Mayer AC, Hardin BE, Scully SR, McGehee MD, Heeney M, McCulloch I (2008) Appl Phys Lett 92:113309
82. Dang MT, Hirsch L, Wantz G (2011) Adv Mater 23:3597–3602
83. Moulé AJ, Tsami A, Brunnagel TW, Forster M, Kronenberg NM, Scharber M, Koppe M, Morana M, Brabec CJ, Meerholz K, Scherf U (2008) Chem Mater 20:4045–4050
84. Moulé AJ, Meerholz K (2007) Appl Phys B 86:771–777
85. Moulé AJ, Meerholz K (2008) Appl Phys B 92:209–218
86. Pettersson LAA, Roman LS, Inganas O (1999) J Appl Phys 86:487–496
87. Chen LM, Hong ZR, Li G, Yang Y (2009) Adv Mater 21:1434–1449
88. Li G, Yao Y, Yang H, Shrotriya V, Yang G, Yang Y (2007) Adv Funct Mater 17:1636–1644
89. Huang DM, Mauger SA, Friedrich S, George SA, Dumitriu-LaGrange D, Yoon S, Moulé AJ (2011) Adv Funct Mater 21:1657–1665
90. Mihailetchi VD, Xie HX, de Boer B, Popescu LM, Hummelen JC, Blom PWM, Koster LJA (2006) Appl Phys Lett 89:012107
91. Chou KW, Yan BY, Li RP, Li EQ, Zhao K, Anjum DH, Alvarez S, Gassaway R, Biocca A, Thoroddsen ST, Hexemer A, Amassian A (2013) Adv Mater 25:1923–1929
92. Li G, Shrotriya V, Yao Y, Huang JS, Yang Y (2007) J Mater Chem 17:3126–3140
93. Yang XN, Loos J, Veenstra SC, Verhees WJH, Wienk MM, Kroon JM, Michels MAJ, Janssen RAJ (2005) Nano Lett 5:579–583
94. Chen D, Nakahara A, Wei D, Nordlund D, Russell TP (2010) Nano Lett 11:561–567

95. Collins BA, Gann E, Guignard L, He X, McNeill CR, Ade H (2010) J Phys Chem Lett 1:3160–3166
96. Roehling JD, Batenburg KJ, Swain FB, Moulé AJ, Arslan I (2013) Adv Funct Mater 23:2115–2122
97. Agostinelli T, Lilliu S, Labram JG, Campoy-Quiles M, Hampton M, Pires E, Rawle J, Bikondoa O, Bradley DDC, Anthopoulos TD, Nelson J, Macdonald JE (2011) Adv Funct Mater 21:1701–1708
98. Yan HP, Swaraj S, Wang C, Hwang I, Greenham NC, Groves C, Ade H, McNeill CR (2010) Adv Funct Mater 20:4329–4337
99. Shin M, Kim H, Park J, Nam S, Heo K, Ree M, Ha CS, Kim Y (2010) Adv Funct Mater 20:748–754
100. Marsh RA, Hodgkiss JM, Albert-Seifried S, Friend RH (2010) Nano Lett 10:923–930
101. Kim S-S, Na S-I, Kang S-J, Kim D-Y (2010) Sol Energ Mat Sol C 94:171–175
102. Watts B, Belcher WJ, Thomsen L, Ade H, Dastoor PC (2009) Macromolecules 42:8392–8397
103. Pingree LSC, Reid OG, Ginger DS (2009) Nano Lett 9:2946–2952
104. Kim HJ, Lee HH, Kim JJ (2009) Macromol Rapid Commun 30:1269–1273
105. Jo J, Kim SS, Na SI, Yu BK, Kim DY (2009) Adv Funct Mater 19:866–874
106. Yun J-J, Peet J, Cho N-S, Bazan GC, Lee SJ, Moskovits M (2008) Appl Phys Lett 92:251912
107. Clarke TM, Ballantyne AM, Nelson J, Bradley DDC, Durrant JR (2008) Adv Funct Mater 18:4029–4035
108. McNeill CR, Halls JJM, Wilson R, Whiting GL, Berkebile S, Ramsey MG, Friend RH, Greenham NC (2008) Adv Funct Mater 18:2309–2321
109. Ayzner AL, Wanger DD, Tassone CJ, Tolbert SH, Schwartz BJ (2008) J Phys Chem C 112:18711–18716
110. Nguyen LH, Hoppe H, Erb T, Gunes S, Gobsch G, Sariciftci NS (2007) Adv Funct Mater 17:1071–1078
111. Zhokhavets U, Erb T, Hoppe H, Gobsch G, Sariciftci NS (2006) Thin Solid Films 496:679–682
112. Warman JM, de Haas MP, Anthopoulos TD, de Leeuw DM (2006) Adv Mater 18:2294–2298
113. Cugola R, Giovanella U, Di Gianvincenzo P, Bertini F, Catellani M, Luzzati S (2006) Thin Solid Films 511:489–493
114. Cho S, Lee K, Yuen J, Wang GM, Moses D, Heeger AJ, Surin M, Lazzaroni R (2006) J Appl Phys 100:114503
115. Kim Y, Choulis SA, Nelson J, Bradley DDC, Cook S, Durrant JR (2005) J Mater Sci 40:1371–1376
116. Kim Y, Choulis SA, Nelson J, Bradley DDC, Cook S, Durrant JR (2005) Appl Phys Lett 86:063502
117. Al-Ibrahim M, Ambacher O, Sensfuss S, Gobsch G (2005) Appl Phys Lett 86:201120
118. Chang L, Lademann HWA, Bonekamp J-B, Meerholz K, Moulé AJ (2011) Adv Funct Mater 21:1779–1787
119. Kumar A, Sista S, Yang Y (2009) J Appl Phys 105:094512
120. Tress W, Leo K, Riede M (2011) Adv Funct Mater 21:2140–2149
121. Müller C, Ferenczi TAM, Campoy-Quiles M, Frost JM, Bradley DDC, Smith P, Stingelin-Stutzmann N, Nelson J (2008) Adv Mater 20:3510–3515
122. Kim JY, Frisbie D (2008) J Phys Chem C 112:17726–17736
123. Pientka M, Dyakonov V, Meissner D, Rogach A, Vanderzande D, Weller H, Lutsen L (2004) Nanotechnology 15:163–170
124. Yan HP, Collins BA, Gann E, Wang C, Ade H, McNeill CR (2012) ACS Nano 6:677–688
125. Collins BA, Ade H (2012) J Electron Spectros Relat Phenomena 185:119–128
126. Zhang Y, Yip HL, Acton O, Hau SK, Huang F, Jen AKY (2009) Chem Mater 21:2598–2600
127. Treat ND, Brady MA, Smith G, Toney MF, Kramer EJ, Hawker CJ, Chabinyc ML (2011) Adv Energy Mater 1:82–89

128. Ruderer MA, Meier R, Porcar L, Cubitt R, Müller-Buschbaum P (2012) J Phys Chem Lett 3:683–688
129. Mauger SA, Chang LL, Friedrich S, Rochester CW, Huang DM, Wang P, Moulé AJ (2013) Adv Funct Mater 23:1935–1946
130. Wodo O, Roehling JD, Moulé AJ, Ganapathysubramanian B (2013) Energy Environ Sci 6:3060–3070
131. He X, Collins BA, Watts B, Ade H, McNeill CR (2012) Small 12:1920–1927
132. Bartelt JA, Beiley ZM, Hoke ET, Mateker WR, Douglas JD, Collins BA, Tumbleston JR, Graham KR, Amassian A, Ade H, Fréchet JMJ, Toney MF, McGehee MD (2013) Adv Energy Mater 3:364–374
133. Collins BA, Tumbleston JR, Ade H (2011) J Phys Chem Lett 2:3135–3145
134. Chirvase D, Parisi J, Hummelen JC, Dyakonov V (2004) Nanotechnology 15:1317–1323
135. Zhang FL, Jespersen KG, Bjorstrom C, Svensson M, Andersson MR, Sundstrom V, Magnusson K, Moons E, Yartsev A, Inganas O (2006) Adv Funct Mater 16:667–674
136. Schmidt-Hansberg B, Sanyal M, Grossiord N, Galagan Y, Baunach M, Klein MFG, Colsmann A, Scharfer P, Lemmer U, Dosch H, Michels J, Barrena E, Schabel W (2012) Sol Energ Mat Sol C 96:195–201
137. Lee JK, Ma WL, Brabec CJ, Yuen J, Moon JS, Kim JY, Lee K, Bazan GC, Heeger AJ (2008) J Am Chem Soc 130:3619–3623
138. Yao Y, Hou JH, Xu Z, Li G, Yang Y (2008) Adv Funct Mater 18:1783–1789
139. Oosterbaan WD, Vrindts V, Berson S, Guillerez S, Douheret O, Ruttens B, D'Haen J, Adriaensens P, Manca J, Lutsen L, Vanderzande D (2009) J Mater Chem 19:5424–5435
140. Martin TP, Wise AJ, Busby E, Gao J, Roehling JD, Ford MJ, Larsen DS, Moulé AJ, Grey JK (2013) J Phys Chem B 117:4478–4487
141. Moulé AJ, Allard S, Kronenberg NM, Tsami A, Scherf U, Meerholz K (2008) J Phys Chem C 112:12583–12589
142. Xin H, Reid OG, Ren GQ, Kim FS, Ginger DS, Jenekhe SA (2010) ACS Nano 4:1861–1872
143. Kietzke T, Neher D, Landfester K, Montenegro R, Guntner R, Scherf U (2003) Nat Mater 2:408–412
144. Erb T, Zhokhavets U, Gobsch G, Raleva S, Stuhn B, Schilinsky P, Waldauf C, Brabec CJ (2005) Adv Funct Mater 15:1193–1196
145. Campoy-Quiles M, Ferenczi T, Agostinelli T, Etchegoin PG, Kim Y, Anthopoulos TD, Stavrinou PN, Bradley DDC, Nelson J (2008) Nat Mater 7:158–164
146. Turner ST, Pingel P, Steyrleuthner R, Crossland EJW, Ludwigs S, Neher D (2011) Adv Funct Mater 21:4640–4652
147. Spano FC (2005) J Chem Phys 122:234701
148. Spano FC (2006) Chem Phys 325:22–35
149. Gierschner J, Huang YS, Van Averbeke B, Cornil J, Friend RH, Beljonne D (2009) J Chem Phys 130:044105
150. Clark J, Chang JF, Spano FC, Friend RH, Silva C (2009) Appl Phys Lett 94:163306
151. Zhao J, Swinnen A, Van Assche G, Manca J, Vanderzande D, Van Mele B (2009) J Phys Chem B 113:1587–1591
152. Wang T, Pearson AJ, Lidzey DG, Jones RAL (2011) Adv Funct Mater 21:1383–1390
153. Pearson AJ, Wang T, Jones RAL, Lidzey DG, Staniec PA, Hopkinson PE, Donald AM (2012) Macromolecules 45:1499–1508
154. Beal RM, Stavrinadis A, Warner JH, Smith JM, Assender HE, Watt AAR (2010) Macromolecules 43:2343–2348
155. van Bavel SS, Barenklau M, de With G, Hoppe H, Loos J (2010) Adv Funct Mater 20:1458–1463
156. Tsoi WC, James DT, Kim JS, Nicholson PG, Murphy CE, Bradley DDC, Nelson J, Kim JS (2011) J Am Chem Soc 133:9834–9843
157. Pascui OF, Lohwasser R, Sommer M, Thelakkat M, Thurn-Albrecht T, Saalwächter K (2010) Macromolecules 43:9401–9410

158. Rivnay J, Noriega R, Northrup JE, Kline RJ, Toney MF, Salleo A (2011) Phys Rev B 83:121306
159. Deibel C, Strobel T, Dyakonov V (2009) Phys Rev Lett 103:036402
160. Guan ZL, Kim JB, Wang H, Jaye C, Fischer DA, Loo YL, Kahn A (2010) Org Electron 11:1779–1785
161. Vandewal K, Tvingstedt K, Gadisa A, Inganas O, Manca JV (2010) Phys Rev B 81:125204
162. van der Hofstad TGJ, Di Nuzzo D, van den Berg M, Janssen RAJ, Meskers SCJ (2012) Adv Energy Mater 2:1095–1099
163. Lee J, Vandewal K, Yost SR, Bahlke ME, Goris L, Baldo MA, Manca JV, Van Voorhis T (2010) J Am Chem Soc 132:11878–11880
164. Braun CL (1984) J Chem Phys 80:4157–4161
165. Wojcik M, Tachiya M (2009) J Chem Phys 130:104107
166. Mihailetchi VD, Koster LJA, Hummelen JC, Blom PWM (2004) Phys Rev Lett 93:216601
167. Mingebach M, Walter S, Dyakonov V, Deibel C (2012) Appl Phys Lett 100:193302
168. Limpinsel M, Wagenpfahl A, Mingebach M, Deibel C, Dyakonov V (2010) Phys Rev B 81:085203
169. Howard IA, Mauer R, Meister M, Laquai F (2010) J Am Chem Soc 132:14866–14876
170. Guo JM, Ohkita H, Benten H, Ito S (2010) J Am Chem Soc 132:6154–6164
171. Kniepert J, Schubert M, Blakesley JC, Neher D (2011) J Phys Chem Lett 2:700–705
172. Kniepert J, Lange I, van der Kaap NJ, Koster LAJ, Neher D (2014) Adv Energy Mater 4:1301401
173. Gluecker M, Foertig A, Dyakonov V, Deibel C (2012) Phys Status Solidi Rapid Res Lett 6:337–339
174. Street RA, Cowan S, Heeger AJ (2010) Phys Rev B 82:121301
175. Cowan SR, Street RA, Cho SN, Heeger AJ (2011) Phys Rev B 83:035205
176. Tsoi WC, Spencer SJ, Yang L, Ballantyne AM, Nicholson PG, Turnbull A, Shard AG, Murphy CE, Bradley DDC, Nelson J, Kim JS (2011) Macromolecules 44:2944–2952
177. Shoaee S, Subramaniyan S, Xin H, Keiderling C, Tuladhar PS, Jamieson F, Jenekhe SA, Durrant JR (2013) Adv Funct Mater 23:3286–3298
178. Jamieson FC, Domingo EB, McCarthy-Ward T, Heeney M, Stingelin N, Durrant JR (2012) Chem Sci 3:485–492
179. McMahon DP, Cheung DL, Troisi A (2011) J Phys Chem Lett 2:2737–2741
180. Pensack RD, Asbury JB (2010) J Phys Chem Lett 1:2255–2263
181. Pensack RD, Guo CH, Vakhshouri K, Gomez ED, Asbury JB (2012) J Phys Chem C 116:4824–4831
182. Caruso D, Troisi A (2012) Proc Natl Acad Sci USA 109:13498–13502
183. Vandewal K, Albrecht S, Hoke ET, Graham KR, Widmer J, Douglas JD, Schubert M, Mateker WR, Bloking JT, Burkhard GF, Sellinger A, Fréchet JMJ, Amassian A, Riede MK, McGehee MD, Neher D, Salleo A (2014) Nat Mater 13:63–68
184. Barbour LW, Hegadorn M, Asbury JB (2007) J Am Chem Soc 129:15884–15894
185. Mauer R, Howard IA, Laquai F (2010) J Phys Chem Lett 1:3500–3505
186. Credgington D, Durrant JR (2012) J Phys Chem Lett 3:1465–1478
187. Wetzelaer G, Kuik M, Blom PWM (2012) Adv Energy Mater 2:1232–1237
188. Pivrikas A, Juska G, Mozer AJ, Scharber M, Arlauskas K, Sariciftci NS, Stubb H, Osterbacka R (2005) Phys Rev Lett 94:176806
189. Shuttle CG, O'Regan B, Ballantyne AM, Nelson J, Bradley DDC, Durrant JR (2008) Phys Rev B 78:113201
190. Deibel C, Baumann A, Dyakonov V (2008) Appl Phys Lett 93:163303
191. Ferguson AJ, Kopidakis N, Shaheen SE, Rumbles G (2011) J Phys Chem C 115:23134–23148
192. Mauer R, Howard IA, Laquai F (2011) J Phys Chem Lett 2:1736–1741
193. Leong WL, Cowan SR, Heeger AJ (2011) Adv Energy Mater 1:517–522
194. Garcia-Belmonte G, Guerrero A, Bisquert J (2013) J Phys Chem Lett 4:877–886

195. Guo JM, Ohkita H, Yokoya S, Benten H, Ito S (2010) J Am Chem Soc 132:9631–9637
196. Nelson J (2003) Phys Rev B 67:155209
197. Shuttle CG, Hamilton R, Nelson J, O'Regan BC, Durrant JR (2010) Adv Funct Mater 20:698–702
198. Rauh D, Deibel C, Dyakonov V (2012) Adv Funct Mater 22:3371–3377
199. Clarke TM, Jamieson FC, Durrant JR (2009) J Phys Chem C 113:20934–20941
200. Koster LJA, Mihailetchi VD, Blom PWM (2006) Appl Phys Lett 88:052104
201. Groves C, Greenham NC (2008) Phys Rev B 78:155205
202. Shuttle CG, O'Regan B, Ballantyne AM, Nelson J, Bradley DDC, de Mello J, Durrant JR (2008) Appl Phys Lett 92:093311
203. Deibel C, Wagenpfahl A, Dyakonov V (2009) Phys Rev B 80:075203
204. Kirchartz T, Nelson J (2012) Phys Rev B 86:165201
205. Hamilton R, Shuttle CG, O'Regan B, Hammant TC, Nelson J, Durrant JR (2010) J Phys Chem Lett 1:1432–1436
206. Shuttle CG, Maurano A, Hamilton R, O'Regan B, de Mello JC, Durrant JR (2008) Appl Phys Lett 93:183501
207. Shuttle CG, Hamilton R, O'Regan BC, Nelson J, Durrant JR (2010) Proc Natl Acad Sci USA 107:16448–16452
208. Goodman AM, Rose A (1971) J Appl Phys 42:2823–2830
209. Mihailetchi VD, Wildeman J, Blom PWM (2005) Phys Rev Lett 94:126602
210. Ma W, Kim JY, Lee K, Heeger AJ (2007) Macromol Rapid Commun 28:1776–1780
211. Tamura H, Burghardt I (2013) J Am Chem Soc 135:16364–16367

Author Queries

Chapter No.: 289

Query Refs.	Details Required	Author's response
AU1	Please consider changing "draw" to "design"	
AU2	Please check that added description of P3HT:PCBM is appropriate	
AU3	Please check that change of "morphology/structure features" to "morphology and structural features" is ok	
AU4	Please check that addition of "the number of" is ok.	
AU5	Please confirm that Sect. 3 is meant here.	
AU6	Please confirm that addition of Fig. 6 is correct	
AU7	Fig. 8 legend: Please check that deletion of "of the solution" is ok	
AU8	Please confirm that addition of "in the rows" is ok	
AU9	Fig. 17d: Please say what the shaded areas in part d signify	
AU10	Fig. 19d: Please say what the Inset shows	
AU11	Please check that re-arrangement of this sentence is ok	
AU12	Please check that change from IV to I/V is ok.	
AU13	The reference [157] is duplicate of reference [62]. Therefore it has been deleted and subsequent references and citations are renumbered. Please check.	
AU14	Please check updates to refs [12] and [66]	